

Toolbox

SpatTrack: An Imaging Toolbox for Analysis of Vesicle Motility and Distribution in Living Cells

Frederik W. Lund^{1,4}, Maria Louise V. Jensen¹, Tanja Christensen¹, Gitte K. Nielsen², Christian W. Heegaard³ and Daniel Wüstner^{1*}

¹Department of Biochemistry and Molecular Biology, University of Southern Denmark, DK-5230 Odense M, Denmark

²Department of Biomedicine, University of Aarhus, DK-8000 Aarhus C., Denmark

³Department of Molecular Biology and Genetics, University of Aarhus, DK-8000 Aarhus C., Denmark

⁴Department of Biochemistry, Weill Medical College of Cornell University, York Ave. 1300, 10065 NY, USA

*Corresponding author: Daniel Wüstner, wuestner@bmb.sdu.dk

Abstract

The endocytic pathway is a complex network of highly dynamic organelles, which has been traditionally studied by quantitative fluorescence microscopy. The data generated by this method can be overwhelming and its analysis, even for the skilled microscopist, is tedious and error-prone. We developed SpatTrack, an open source, platform-independent program collecting a variety of methods for analysis of vesicle dynamics and distribution in living cells. SpatTrack performs 2D particle tracking, trajectory analysis and fitting of diffusion models to the calculated mean square displacement. It allows for spatial analysis of detected vesicle patterns including calculation of the radial distribution function and particle-based colocalization. Importantly, all analysis tools are supported by Monte Carlo simulations of synthetic images. This allows the user to assess the reliability of the analysis and to study alternative scenarios. We demonstrate the functionality of SpatTrack by

performing a detailed imaging study of internalized fluorescence-tagged Niemann Pick C2 (NPC2) protein in human disease fibroblasts. Using SpatTrack, we show that NPC2 rescued the cholesterol-storage phenotype from a subpopulation of late endosomes/lysosomes (LE/LYSs). This was paralleled by repositioning and active transport of NPC2-containing vesicles to the cell surface. The potential of SpatTrack for other applications in intracellular transport studies will be discussed.

Keywords Bayesian, cholesterol efflux, convex hull, lysosome, Monte Carlo, Niemann Pick disease, particle tracking, pattern analysis, radial distribution function, spatial statistics

Received 13 March 2014, revised and accepted for publication 17 September 2014, uncorrected manuscript published online 22 September 2014, published online 16 October 2014

Endocytosis of proteins from the cell surface and subsequent sorting of internalized cargo in endosomes is a complex and highly dynamic process. Traditionally, endocytosis has been studied by subcellular fractionation and by transmission electron microscopy after suitable labeling of endocytic ligands (1,2). In parallel, fluorescence microscopy has evolved as a major tool to study the endocytic pathway. This is a consequence of the high specificity and sensitivity of fluorescence and the relative ease of labeling endocytic cargo with small fluorescent probes.

Moreover, only fluorescence studies of the endocytic pathway bear the potential of measuring biophysical properties of the endosome, like pH or concentration of ions like calcium and chloride (3,4). Ligands of endocytic receptors have several fates once arrived in the endosome; they can recycle to the cell surface from early sorting or recycling endosomes, like transferrin after releasing iron into the endosomal lumen (5). They can become targeted to the trans-Golgi network in a retrograde trafficking route, as furin or several plant toxins (5,6). Ligands can be also

transported to late endosomes and lysosomes (LE/LYSs) for degradation, as, for example, low-density lipoprotein (LDL) particles (7), or they can fulfill some function as resident protein in these organelles, like, for example, Niemann Pick C2 protein being involved in cholesterol export from LE/LYSs (8).

Major properties of the endocytic and secretory pathway have been elucidated by quantitative fluorescence microscopy combined with digital image analysis already more than 20 years ago. Examples include iterative fractionation of recycling ligands from cargo destined for lysosomal degradation within the sorting endosome (9), maturation of sorting into LE by diminishing fusion competence (10), retrograde tracking of transferrin between early endosomes (11) and the kinetics of acidification along the endocytic pathway (12). Similarly, vesicle tracking along the secretory pathway has been intensively investigated using quantitative time-lapse microscopy (13–16). Despite this obvious potential of the method, quantitative imaging approaches for studying the endocytic and secretory pathway are limited, and a large body of published work uses fluorescence microscopy only in a very qualitative manner. Some selected images are shown as being representative for the behavior in a whole cell population. Although very popular, this is a very questionable approach, given the dynamic and heterogeneous distribution of the investigated molecules. To make quantitative imaging accessible for a broader community of cell biologists, many software packages have been developed in recent years. For example, several programs exist for single or multiple particle tracking including SpotTracker (17) and Particle Tracker (18) for ImageJ (<http://imagej.nih.gov/ij/>), MTT for MatLab (19) and Imaris Track developed by Bitplane (<http://www.bitplane.com/>). None of these tracking programs extract information about spatial vesicle patterns from the acquired image sequences. A recently published plugin to ImageJ and Fiji (<http://fiji.sc/Fiji>), named MosaicIA, does perform a spatial analysis of two vesicle populations by determining their respective nearest neighbor (NN) distances and inferring the most likely NN interaction potential (20,21). However, this program allows neither for spatial analysis of a single vesicle population in the cell geometry nor for parallel tracking of vesicles in time series. Neither does it provide other measures of

particle patterns than the NN distance. Other programs and algorithms were dedicated to the analysis of probe coincidence within the cell and for determining shared transport routes of endocytic cargo. Examples out of the large variety of such freely available colocalization analysis programs are the JaCoP plugins to ImageJ collecting a number of published algorithms (22), the OBCOL plugin to ImageJ (23), the Squash plugin to ImageJ (24) and some pixel-based correlation tools developed in MatLab (The MathWorks Inc.) (25,26). These programs, however, do not allow for assessing dynamic properties of the investigated fluorescent molecules and do not provide information about the position of detected colocalizing molecules within the cellular context.

Here we present SpatTrack, a program combining multiple algorithms for particle tracking and analysis from two-dimensional cell images. SpatTrack performs reliable vesicle tracking and fitting of the mean square displacement of particles to various diffusion/transport models. It also contains add-ons for assessing the spatial statistics of the tracked particle populations in the cell geometry based not only on the NN measure but also by using the radial distribution function (RDF). In addition, SpatTrack performs object-based colocalization analysis, which is directly comparable to the results obtained by two-color RDF calculation. In SpatTrack, graphical user interfaces (GUIs) are implemented for all subroutines and connected to the main tracking program. This provides the possibility to analyze tracked intracellular particles in a variety of ways without any programming knowledge. Batch processing of image data allows for the execution of repeated image processing tasks without manual user intervention. Our program is free for download and well documented in the accompanying user guide. We use SpatTrack to determine the mobility and spatial distribution of internalized fluorescent NPC2 in NPC2-deficient human skin fibroblasts. Other potential applications of SpatTrack are discussed.

Results

Particle tracking and trajectory analysis using SpatTrack
 Many different computational schemes have been developed over the last 15–20 years for particle tracking in microscope image sequences. The typical work flow a

acquisition of the time-lapse data involves (i) image pre-processing (registration, shading correction and possibly denoising to enhance spot visibility) followed by (ii) spot detection in the individual image frames and (iii) linking of the detected spots to obtain the trajectories of each moving particle (27,28). Existing routines differ in all aspects of this work flow, and for every task, a different combination of methods might be appropriate. Particle tracking in SpatTrack is based on a publicly available tracking program written by Crocker and Grier for IDL based on the NN method for particle linking (29). This routine was later ported to MatLab by Blair and Dufresne and is available at <http://physics.georgetown.edu/matlab/>. Here we have incorporated the existing MatLab files into a user-friendly GUI (see the accompanying user guide to the program). Furthermore, we have connected the tracking part with tools for trajectory and pattern analysis, as discussed below. We have recently performed an extensive testing of the tracking performance of SpatTrack using simulated images with diffusing particles, fluorescent beads and intracellular vesicles (30). This study demonstrated that the tracking routine in SpatTrack can recover diffusion constants of particles in the presence of noise (additive and multiplicative), photobleaching and illumination shading with high accuracy. We showed that image denoising using the boxcar filter as well as the adaptive threshold, which weights the threshold by the mean intensity in each frame, gave accurate results even for endosome-like particles with changing shape (30). From this, we conclude that SpatTrack is on par with other freely available tracking algorithms. Particle tracking with SpatTrack is described in detail in the accompanying user guide.

After recording particle positions over time, the trajectories can be further analyzed in SpatTrack using the add-on for trajectory analysis (Figure 1A). Trajectories may either be loaded directly from the tracking program or from properly formatted text files. The latter option allows the user to record trajectories in another tracking program and to perform the trajectory analysis in SpatTrack if he/she should so desire. For further information about formatting text files, we refer to the user guide accompanying the program. Fitting the mean squared displacement (MSD) of a particle trajectory is a commonly used method to acquire diffusion constants and/or flow components from

particle trajectories. The MSD is calculated as

$$\text{MSD}(t) = \frac{1}{N-n} \sum_{i=1}^{N-n} \left\{ (x(i) - x(i+t))^2 + (y(i) - y(i+t))^2 \right\}, \quad (1)$$

where N is the number of frames, h is the time between subsequent frames and Δt is the time lag corresponding to n frames. The MSD is the second moment, i.e. the variance, of the probability density function (PDF) of the underlying stochastic process. The PDF equals the step length distribution in tracking of randomly moving particles. Its time evolution is governed by the diffusion equation and is also called the propagator of the studied diffusion process. Analysis of the MSD is valid, provided that the distribution of step lengths is Gaussian, which is true for many types of random walks including Brownian motion, some forms of subdiffusion and Brownian motion plus flow. The MSD may be fitted to analytical models for pure Brownian diffusion:

$$\text{MSD}(t) = 4Dt, \quad (2)$$

or diffusion plus flow:

$$\text{MSD}(t) = 4Dt + v^2t^2. \quad (3)$$

Here, D is the diffusion constant, v is the velocity and t is the time lag. The model in eqn 3 is often used in cell biology to describe the motion associated with active transport of endosomes (31) or virus particles (32). Many tracking studies of intracellular organelles reveal anomalous diffusion (33–35), being implemented in SpatTrack as:

$$\text{MSD}(t) = 4D_\alpha t^\alpha. \quad (4)$$

Here, the anomalous exponent, α , depends on the type of anomalous diffusion: $0 < \alpha < 1$ for anomalous subdiffusion and $1 < \alpha < 2$ for anomalous superdiffusion. Anomalous subdiffusion is common in living cells likely because of organelles and vesicles being caught in the cytoskeleton meshwork and partly because of molecular crowding by other macromolecules (35–37). To describe the transition from anomalous subdiffusion on short times to directed diffusion on longer time scales, we set up an extended model for anomalous diffusion including a component for directed diffusion (38):

$$\text{MSD}(t) = 4D_\alpha t^\alpha + v^2t^2. \quad (5)$$

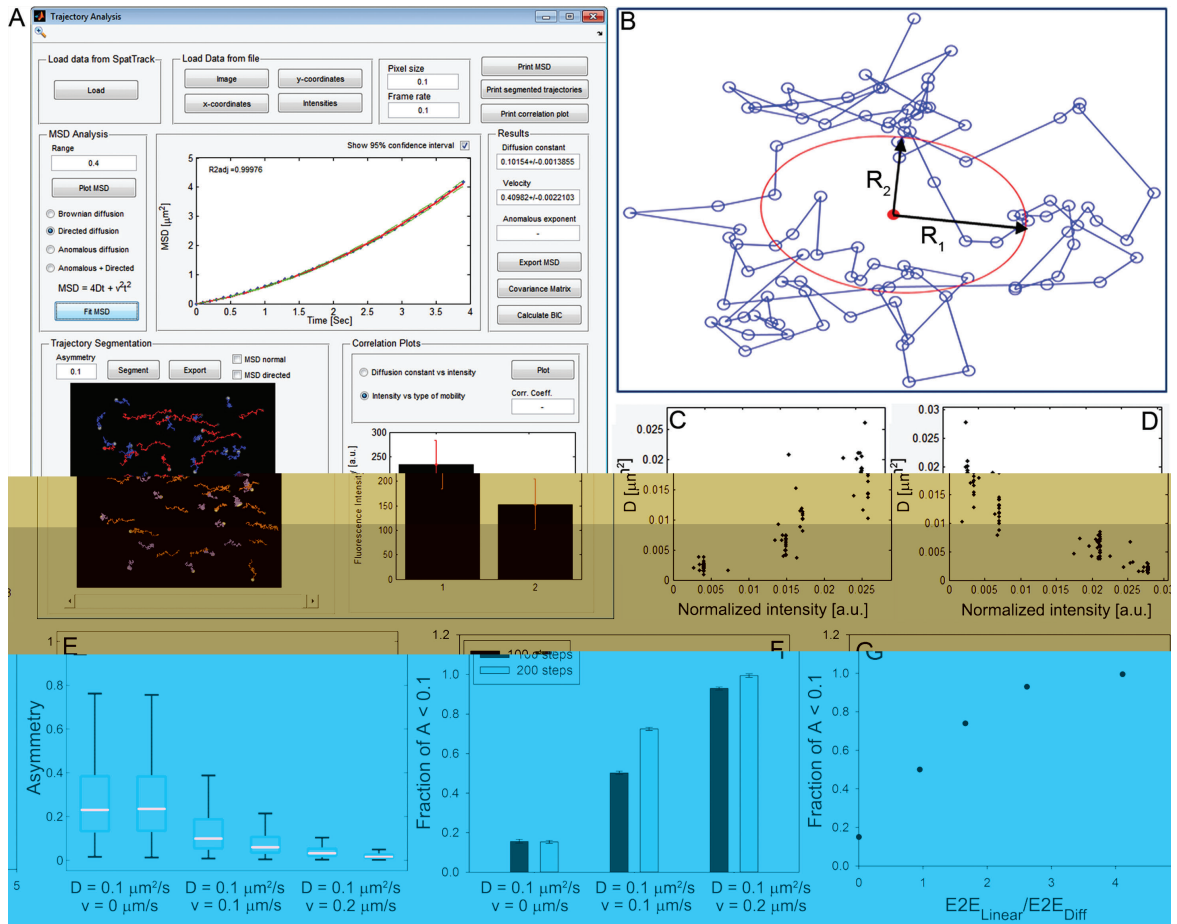


Figure 1: GUI and validation of trajectory analysis. Once the x-, y-coordinates and fluorescence intensity of particles are determined, the statistical features of trajectories can be analyzed. In the GUI for trajectory analysis, the MSD is calculated and can be fitted to different diffusion models (A, upper plot). Trajectories may be separated into directed trajectories and trajectories of normal/hindered diffusion (lower left plot). Trajectory separation is based on the RoG (see main text), which is shown in red on top of an example trajectory in (B). After the separation of trajectories displaying either normal/hindered diffusion or diffusion plus flow, it is possible to generate a plot of the average fluorescence intensity of the particles in each group (A, lower right corner). Alternatively, one may examine the correlation between the diffusion constant and fluorescence intensity of each particle. This is shown for cases of positive and negative correlation in (C) and (D), respectively. These plots were generated from simulated images with four different particle types with different diffusion constants and different fluorescence intensities. E–G), validation of the RoG analysis by additional Monte Carlo simulations of vesicle motility as described in the text. E) Asymmetry values calculated from 10 000 trajectories of 100 steps in the absence or presence of a flow component along the x-direction. F) Fraction of simulated trajectories classified as diffusion + flow by the criterion $A < 0.1$ (eqn 6) for different trajectory lengths and flow components. G) The same parameter as in (F) is plotted as function of the ratio of end-to-end distances of trajectories simulated with Brownian motion ($E2E_{Diff}$) or active transport ($E2E_{Linear}$).

is model is implemented in SpatTrack and will also be useful in samples containing subpopulations of particles moving by con ned and directed transport.

From eqn 1, it is apparent that as the lag time, t , increases, the number of statistically independent displacement

samples decreases. us, the statistical signi cance of the MSD decreases with increasing lag time (39). Furthermore, the statistical signi cance of the MSD decreases for short trajectories, as the number of trajectory segments for each lag time depends on the total number of steps in the trajectory. SpatTrack was primarily developed for

tracking relatively short trajectories (i.e. trajectories of a few hundred steps). Therefore, to increase the significance of the fitted parameters, we chose to fit the ensemble averaged MSD of all trajectories rather than the MSD of single trajectories. In addition, SpatTrack shows the fitted curves with 95% confidence intervals and provides the fitted parameter values as mean \pm standard error (SE). It also contains an option to show the covariance matrix for the parameters, which will reveal eventual dependencies in the parameter estimation. Low off-diagonal values in the parameter covariance matrix indicate low dependencies and are one indication for a good fit quality (40). Figure 1A shows the averaged MSD of 60 trajectories recovered by SpatTrack from a simulated image sequence in which some particles were moving by normal diffusion, while others moved by directed transport. We included an option to fit a portion of the MSD only, for example the plot shows the first 4/5th of the MSD (Figure 1A, blue dots) which was fitted to eqn 3 modeling diffusion + transport (Figure 1A, red line). Finally, the fit is shown with 95% confidence intervals (Figure 1A, green dashed lines). In addition to MSD analysis, it is possible to pool the trajectories into normal/conditioned trajectories and directed trajectories. This pooling is based on the radius of gyration (RoG) of the individual trajectories. Consider a trajectory of a moving particle in a coordinate system with origin in the trajectory's center of mass (Figure 1B). The shape of the trajectory may be described by an ellipse with a larger and smaller principal radius (R_1 and R_2) which together form the RoG. The term stems from its mathematical equivalence (in two dimensions) to the principal axes of the inertia tensor of a rigid body. Like the MSD, the tensor of gyration is a second-order statistic. While the MSD is given by the diagonal elements of the covariance matrix (the variances), the gyration tensor also includes the off-diagonal elements (the covariances), thereby providing information about possible correlations in the diffusion steps of a particle. Note that this is a different covariance matrix than discussed above; here, covariance refers to the position of detected particles, while above covariance was calculated between the estimated parameters of the regression model. Given that the distribution of step sizes is Gaussian, the RoG is a convenient method to analyze the asymmetry of a trajectory (determined by the asymmetry of the Gaussian-shaped PDF). It is often used as a measure of

point distributions with applications ranging from point tracking, as here, over percolation analysis in polymer physics (41), to mechanics (42) and image description (43). An example trajectory with the ellipse determined by the two principal radii, R_1 and R_2 , is shown in Figure 1B. From the principal radii, the asymmetry of the trajectory is calculated as

$$A = \frac{R_2}{R_1}. \quad (6)$$

For a circular trajectory, $R_1 = R_2$, giving $A = 1$. In the other extreme, for a linear trajectory $R_2 = 0$ giving $A = 0$. Analysis of the asymmetry of moving particles was first described by Saxton who found that for unobstructed Brownian diffusion $A = 0.12$ (44). In addition, trajectory asymmetry was used as a feature for the detection of directed motion in two and three dimensions (45,46). We performed additional particle simulations in SpatTrack to assess the potential of the RoG measure for discriminating different vesicle populations (Figure 1E–G). Diffusion was simulated with steps of random (walking point) length in the x - and y -direction. For diffusion plus active transport, a constant value corresponding to the velocity term was added in the x -direction. For the analysis shown in Figure 1E, we chose a box-and-whisker plot, which is a convenient representation of the location and variability of a given data set (47). It shows a box defined by the lower and upper 25th (q_1) and 75th (q_3) percentiles, and the median being marked by a subdivision of the box (red straight lines in blue boxes in Figure 1E). The whiskers extend to the most extreme data points not considered outliers. More specifically, if the maximum whisker length is w , then the default is a w of 1.5. Outliers are defined as values larger than $q_3 + w(q_3 - q_1)$ or smaller than $q_1 - w(q_3 - q_1)$ corresponding to ± 2.7 standard deviations (SDs) or 99.3 coverage if the data are normally distributed. Note that the plots shown in Figure 1E do not show outliers.

From such simulations, we found that about 15% of trajectories of particles moving only by Brownian diffusion (i.e. no active transport) have $A < 0.1$, irrespective of the trajectory length. Unfortunately, this means that a fraction of trajectories from normal diffusion will always be misclassified as containing a component of directed transport. To investigate this further, we simulated 10 000

trajectories of particles moving by diffusion plus flow with a fixed diffusion constant but variable velocity. For each parameter combination, we determined the relative contribution of the diffusive component and the flow component on the particles' total displacement. The contribution of the diffusive component was determined by the average end-to-end distance for particles moving by Brownian diffusion alone, where the end-to-end distance is the shortest distance between the first and the last point in a trajectory. For trajectories moving by diffusion plus flow, the contribution of the flow was calculated as the difference between the end-to-end distance of trajectories moving by diffusion alone and the end-to-end distance of trajectories moving by diffusion plus flow. For example, for particles moving by diffusion alone with a diffusion constant of $0.1 \mu\text{m}^2/\text{second}$ the end-to-end distance was $5.61 \mu\text{m}$, while for particles moving by diffusion plus flow with a diffusion constant of $0.1 \mu\text{m}^2/\text{second}$ and a velocity of $0.2 \mu\text{m}/\text{second}$ the end-to-end distance was $20.30 \mu\text{m}$. Thus, the contribution by the flow component was $20.30 \mu\text{m} - 5.61 \mu\text{m} = 14.69 \mu\text{m}$. Secondly, we calculated the relative contributions of the flow component compared to the diffusional motion by the ratio $R_{E2E} = E2E_{\text{Linear}}/E2E_{\text{Di}}$, where $E2E_{\text{Linear}}$ and $E2E_{\text{Di}}$ are the end-to-end distances due to flow and diffusional motion, respectively. Accordingly, for trajectories where flow is the dominant cause of displacement $E2E_{\text{Linear}} > E2E_{\text{Di}}$ and the ratio $R_{E2E} > 1$, while for trajectories where the diffusive motion is the dominant cause of displacement, $E2E_{\text{Linear}} < E2E_{\text{Di}}$, and the ratio $R_{E2E} < 1$. Plotting the fraction of trajectories with $A > 0.1$ for each parameter combination as a function of R_{E2E} shows that for increasing velocity with respect to the diffusion constant, where $E2E_{\text{Linear}}$ is increasingly larger than $E2E_{\text{Di}}$, the fraction of correctly classified trajectories approaches 1 (Figure 1G).

Thus, the RoG is a sensitive measure for detecting active transport but has in our hands a false-positive error of about 15% (see above). In addition, the simulations show that more trajectories of particles with diffusion plus flow

Alexa546-NPC2, as a measure of vesicle cargo content, and vesicle mobility (not shown). Still, we believe that this option is useful for many applications; more of them will be introduced in the *Discussion* section. SpatTrack can also accurately detect particles with different motion characteristics but comparable intensity (not shown, but see 30).

As described above, SpatTrack includes models for four different types of diffusion (i) Brownian diffusion, (ii) Brownian diffusion plus flow, (iii) anomalous diffusion and (iv) anomalous hindered diffusion plus flow. The latter model can describe one population with both characteristics on two different time scales, or two particle populations where one population is moving by anomalous hindered diffusion and the other by flow (38). Choosing the correct model to describe the type of diffusion is not trivial. Typically, a model with more free parameters will yield a better fit (i.e. a fit with lower residuals). However, increasing the number of free parameters comes at the risk of overfitting. That is, while the extra free parameters improve the fitted curve with respect to the data, they provide no additional information about the underlying process. Several statistical methods are available for model selection, and we chose to implement the Bayesian information criterion (BIC) into SpatTrack. The BIC, also called Schwartz Bayesian criterion, is an approximation of a Bayesian model selection analysis and is defined as follows (50,51):

$$\text{BIC} = n \cdot \ln \left(\frac{\text{RSS}}{n} \right) + K \cdot \ln(n). \quad (7)$$

Here, K is the number of free parameters of the selected model, n is the number of data points, and RSS is the sum of squared residuals between data and model. The RSS represents the maximized likelihood of an estimated model, assuming that the model errors are normally distributed. Generally, a good fit results in low RSS values meaning that the likelihood of the chosen model to resemble the data is high (40). On the other hand, elaborated models with more parameters will always give better fits, which has to be weighed against the model complexity. This is exactly what the BIC does by including a penalty term for adding further parameters (i.e. increasing K) to the model. For model selection, we calculate the BIC for all i model fits

and determine

$$\Delta\text{BIC} = \text{BIC}_i - \min \text{BIC}, \quad (8)$$

where $\min \text{BIC}$ refers to the model with the lowest BIC. From that, one can define the Akaike weights, or more precisely, BIC model or Schwartz weights as follows (51,52):

$$w_i = \frac{\exp(-0.5 \cdot \Delta\text{BIC}_i)}{\sum_{j=1}^J \exp(-0.5 \cdot \Delta\text{BIC}_j)}. \quad (9)$$

Here, the sum runs over the total number of candidate models, J . We also calculated and tested the Akaike information criterion, another measure of model adequacy, but found it less decisive than the BIC (not shown), which is in line with previous reports on single-particle tracking data (53). The decision tree shown in Figure 2 was developed to assist the user in choosing the correct model for a given MSD. It thereby follows the philosophy of Türkcan et al. but does not invoke a particular physical motion model entering the calculation of likelihood functions as in their work (53,54). Initially, each of the four models is fitted to the experimental MSD data, and the SE of the fitted value is calculated for each free parameter of the respective model. For a given parameter, the SE is calculated from the 95% confidence interval as follows:

$$\text{SE} = \frac{\text{CI}_{\text{up}} - \bar{x}}{1.96}, \quad (10)$$

where CI_{up} is the upper value of the 95% confidence interval and \bar{x} is the fitted value of the parameter. Models with one or more parameters where SE is more than 10 times larger than the fitted value are automatically excluded from further processing. For example, a fitted velocity of $1 \mu\text{m}/\text{second} \pm 10 \mu\text{m}/\text{second}$ is not informative and will be discarded by SpatTrack. Subsequently, the BIC is calculated for the models with acceptable SEs of the fitted parameters, as given in eqn 7. The BIC penalizes models with more free parameters, and ideally the model with the lowest BIC should be the model with the least parameters which is able to describe the data. However, systematic tests on simulated particle populations showed that the BIC alone is not sufficient to determine the appropriate model (Figure S1, Supporting Information). While the BIC could distinguish between diffusion plus flow and diffusion without flow with more than 80% efficiency, it often failed to distinguish between Brownian diffusion (eqn 2) and anomalous subdiffusion (eqn 4 with $\alpha < 1$) as well as

between Brownian diffusion plus flow (eqn 3) and anomalous diffusion plus flow (eqn 5). This is in line with earlier work showing that the BIC misclassifies trajectories generated using potentials of different conformation strength (i.e. second versus fourth order) (53). Therefore, to ensure reliable and robust model selection, the user should follow the decision tree shown in Figure 2. If the BIC indicates directed motion (second box from top in Figure 2), this could indicate normal diffusion plus flow (eqn 3 and upper right grey box in Figure 2). Alternatively, it could be caused by combined anomalous diffusion and directed transport (eqn 5). If this model is favored by the analysis, one should inspect the estimated anomaly constant, α and additionally perform the RoG analysis. The latter will allow one to decide, whether the model of anomalous diffusion plus flow is favored because of one vesicle population with complex motility behavior or because of two vesicle populations with different motion characteristics (Figure 2). If $\alpha > 1.0$ in the model of anomalous diffusion plus flow (eqn 5) and the RoG indicates one population only, one would have a model of superdiffusion and flow, which both are related processes. In this case, the covariance matrix will likely indicate high correlation between the fitted α and flow parameter, v . Thus, the model of diffusion plus flow (eqn 3) will be sufficient to describe the data and should therefore be favored. If $\alpha < 1.0$ in the model of anomalous diffusion plus flow (eqn 5) and the RoG indicates one population only, one would conclude that this population moves by hindered diffusion (i.e. subdiffusion) plus flow (left grey box at bottom of Figure 2).

It is well possible that the BIC analysis does not favor a model with directed diffusion, in which case, the user should follow the left branch of the decision tree in Figure 2. Here, the BIC could also indicate anomalous diffusion (eqn 4 and third box from top to the left in Figure 2). Because of the statistical uncertainty of the MSD, we found that MSDs for particles moving by Brownian diffusion often show signs of anomalous hindered motion (see Figure S1 and above). However, by analysis of simulated trajectories, we found that the anomalous exponent, α , very rarely was less than 0.9 for Brownian diffusion. Thus, if the BIC indicates anomalous hindered diffusion but the anomaly is close to 1 (i.e. $\alpha > 0.9$), the type of motion is most likely Brownian diffusion. SpatTrack also provides the Akaike weights (eqn 10), which give a number between 0 and 1 and allow for

quick ranking of the various models. The Akaike weights, however, do not provide additional information.

Mobility of LE and LYSs containing fluorescent NPC2

We set out experiments to determine the mobility of NPC2-containing vesicles at different stages of cholesterol efflux using the tools described above. First, we verified that bovine NPC2 is able to rescue the cholesterol-storage phenotype in the disease cells under our experimental conditions. To this end, NPC2-deficient fibroblasts were first grown in normal growth medium with 10% fetal bovine serum (FBS) to accumulate lipoprotein-derived cholesterol in the lysosomal storage organelles (LSOs). Subsequently, cells were grown in growth medium where FBS was exchanged with lipoprotein-deficient serum (LPDS) containing 100 nM NPC2. To quantify the amount of free cholesterol, the cells were labeled with lipin as described in *Materials and Methods*. Figure S2A shows an example of a lipin-labeled cell at the beginning of the experiment, while Figure S2B shows an example after additional 48 h of growth in LPDS without functional NPC2. In Figure S2C, a cell is shown after 48 h of growth in LPDS-supplemented medium with 100 nM functional NPC2. Clearly, NPC2 reduced lipin intensity in the LSOs significantly. We calculated the fraction of integrated lipin intensity in the LSOs with respect to the total integrated lipin intensity of the cells. This is shown in Figure S2D after 0 and 48 h incubation in LPDS, in the presence and absence of NPC2. Next, we quantified the uptake and recycling kinetics of Alexa488-NPC2, showing that the majority of the protein becomes retained in the LE/LYSs labeled with Rh-dextran (Figure S2E–G). Fluorescent NPC2 was also able to correct the cholesterol-storage phenotype (Figure S5). Note that NPC2 purified from bovine milk using the same protocol as here was found to strongly reduce the cholesterol-storage phenotype *in vivo*, i.e. in liver, spleen, kidney and lung of NPC2 knockout mice (55). Similarly, disease-associated macrophage infiltration in affected tissues was diminished (55). Together, we ensured that the NPC2 used in this study can rescue the cholesterol-storage phenotype and is therefore functional. Most of the vesicles containing fluorescent NPC2 in disease fibroblasts are LYSs, while some will likely be endosomes formed by endocytosis of NPC2 protein from the plasma membrane (PM). For the sake of clarity, we do not further distinguish between these populations and call all NPC2-containing

Decision tree for the type of diffusion

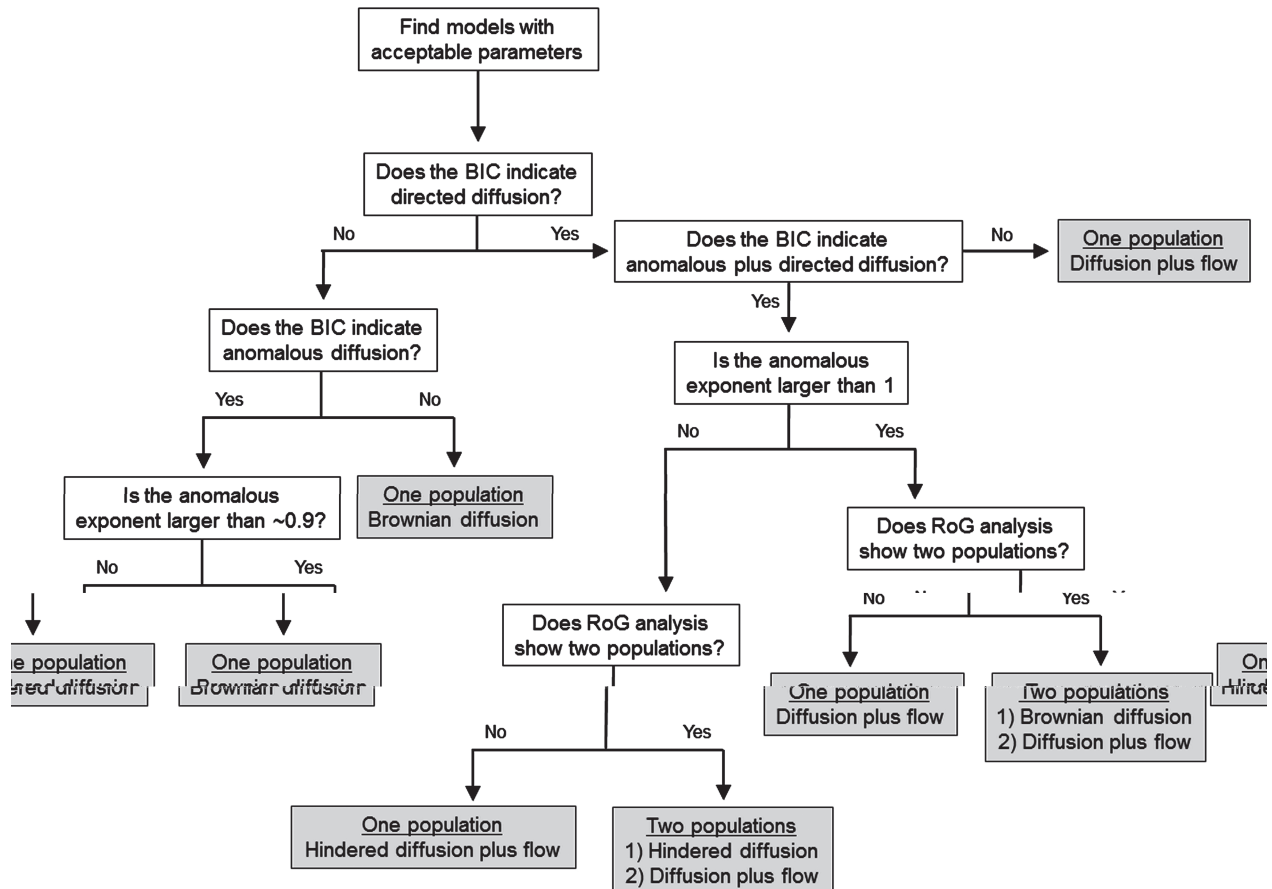


Figure 2: Decision tree for selection of a suitable motion model. After calculating the MSD from all tracked particle trajectories, SpatTrack allows for fitting four different motion models, i.e. Brownian diffusion (eqn 2), Brownian diffusion plus flow (eqn 3), anomalous diffusion (eqn 4) or anomalous diffusion plus flow (eqn 5). The SE of each estimated parameter is calculated for each model used for fitting, and only models in which $\text{SE} < 10$ times the mean value of the fitted parameter are retained or ‘acceptable’ (see first box on top). The BIC defined in eqn 7 and the RoG analysis, providing an expression for the asymmetry of the trajectories (A in eqn 6) are subsequently used for finding the model that describes the MSD data best (see text for further explanations).

vesicles for LE/LYSs. This is justified by their strong overlap with Rh-dextran (Figure S2), a marker for the degradative endocytic pathway (4,5). We tracked the LE/LYSs containing Alexa488-NPC2 using the SpatTrack particle tracking submenu, presented above, in image stacks of 100 frames. In total, this yielded 1039 full-length trajectories (i.e. trajectories of 100 steps) from 9 cells at 24 h of incubation and 1972 trajectories from 10 cells at 48 h. To get a sufficiently large data set, all respective trajectories from 24 or 48 h were pooled, and the MSDs were analyzed by fitting them to all four models of vesicle transport (see eqns 2–5 and above). Next, we compared the fit quality for

all four models based on the SE, 95% confidence intervals and covariance matrix. Finally, we analyzed the BIC, ΔBIC and Akaike weights as described above in eqns 2–5, which revealed that the model for anomalous diffusion plus flow, eqn 5 is most appropriate to describe the data (see Table 1).

The other models given in eqns 2–4 could not adequately describe the data, as was inferred from the information criteria and following the decision tree. For example, the model of normal diffusion fails to describe the MSD data, despite rather low confidence intervals (Figure 3A, inset).

The MSDs and fitted curves for the model of anomalous diffusion plus flow are shown in Figure 3A, where the blue

curve is the plot of eqn 5 for 24 h, while the red curve is for 48 h of incubation (see ts in Figure 3A shown with the respective 95% confidence interval, dashed green lines). The estimated anomaly parameter was $\alpha = 0.66$ for both time-points, enabling us to directly compare

Table 1: MSD data for vesicles containing Alexa488-NPC2 after 24 and 48 h of incubating cells with the protein were analyzed using the model of normal diffusion (eqn 2), normal diffusion plus flow (eqn 3), anomalous diffusion (eqn 4) or anomalous diffusion plus flow (eqn 5)

	Normal diffusion	Normal diffusion plus flow	Anomalous diffusion	Anomalous diffusion plus flow
<i>24 h</i>				
BIC	−404.162	−579.773	−516.097	−685.688
ΔBIC	281.5261	105.9143	169.5911	0.000
Akaike weights	7.369e−62	1.002e−23	1.492e−37	1.000
<i>48 h</i>				
BIC	−217.835	−536.972	−433.846	−659.368
ΔBIC	441.533	122.396	225.521	0.000
Akaike weights	1.325e−96	2.642e−27	1.068e−49	1.00

The BIC, ΔBIC and Akaike weights were calculated according to eqns 7, 8 and 9, respectively. The model with the lowest BIC, giving ΔBIC equal to zero and Akaike weights of unity, is chosen as the preferred model (see text for further explanations).

4 pixels. Assuming that the particles do not overlap, this is a valid approach, as endosomes do have a physical size. However, this is not true for a distribution of random points.

Therefore, the user must supply the approximate particle size used during particle detection/tracking to ensure that the randomly generated particles have the same minimum inter-particle distance. For example, if the estimated particle size used for tracking was 4 pixels, the minimum possible particle–particle distance is also 4 pixels. As this is not true for a randomly generated point distribution, the user must supply the estimated particle size used for tracking to ensure that the random particles have the same minimum inter-particle distance (see Figure 4).

The second method for spatial pattern analysis (SPA) is measuring the NN distance between each particle and its NN (20,21). This method is useful to determine whether particles accumulate or repulse each other or are randomly distributed. The minimum, maximum and mean NN distances as well as the variance of the NN distances are determined for the tracked particles and the random point distribution (see GUI in Figure S3A). In addition, the add-on returns the average NN ratio (ANN) given by

$$\text{ANN} = \frac{\langle \text{NN}_{\text{obs}} \rangle}{\langle \text{NN}_{\text{rand}} \rangle}, \quad (11)$$

where $\langle \text{NN}_{\text{obs}} \rangle$ and $\langle \text{NN}_{\text{rand}} \rangle$ are the mean NN distances, over all tracked or randomly generated particles, respectively. The ANN indicates whether the particles are clustered or dispersed: for $\text{ANN} < 1$ the particles exhibit clustering, while for $\text{ANN} > 1$ the particles are dispersed. Because of relatively low number of tracked particles in a cell, we found that performing the calculation several times for the same data yielded slightly different results.

These differences occur because the number of randomly distributed points is initially equal to the number of detected vesicles per cell and therefore relatively small (i.e. in the range of 150–200). To improve the statistical accuracy, we included an option to determine the number of simulations that enter the mean in the final results on the ANN parameter (see eqn 11). This approach is common in statistical analysis of experimental data and is generally referred to as a (naive) Monte Carlo simulation (see, for example, 40, 57, 58). In SpatTrack, the random point distribution is generated in such a manner that any location has equal probability of receiving a point and the points are independent from each other. Assuming that the tracked particles are also randomly distributed, the confidence interval for the Monte Carlo simulation is given by, $\text{CI} = 1 - (1/s)$, where s is the number of Monte Carlo iterations. Hence, for a 95% confidence interval, we tested the observed distribution against 20 simulated distributions (14). Then the reported values were the mean values of these 20 simulated particle distributions. The final ANN averaged over the number of Monte Carlo cycles is thus given by

$$\overline{\text{ANN}} = \frac{1}{n} \sum_{i=1}^n \frac{\langle \text{NN}_{\text{obs}} \rangle}{\langle \text{NN}_{\text{rand}} \rangle_i}, \quad (12)$$

where $\langle \text{NN}_{\text{rand}} \rangle_i$ is the average NN distance of the i th random point distribution and $\overline{\text{ANN}}$ is the average NN distance over n Monte Carlo cycles. To further verify the statistical significance of SpatTrack reports the SD of the n calculations. In addition to the NN analysis, this add-on calculates the fractional area occupied by the tracked particles in the cell. This is an independent measure of the degree of vesicle aggregation/dispersion. This area

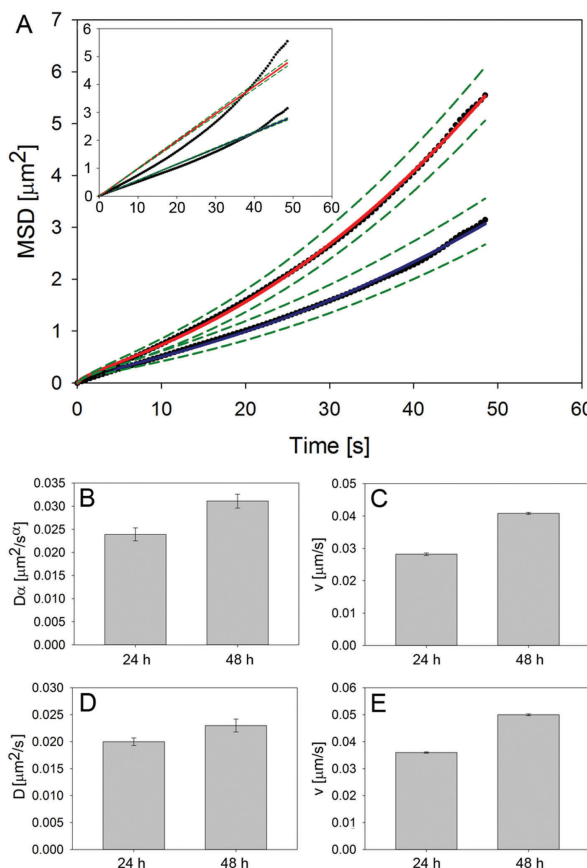


Figure 3: Motility analyses of NPC2-containing vesicles in disease fibroblasts. NPC2 disease fibroblasts were cultured in medium containing LDL and other lipoprotein sources before switching to medium containing LPDS and 100 nM Alexa546-NPC2 for 24, 48 h. Cells were washed and imaged on a temperature-controlled spinning disk microscope. Vesicles containing Alexa546-NPC2 were tracked using SpatTrack, and trajectories were analyzed using the respective GUI (see Figure 1) and the strategy outlined in the decision tree of Figure 2. A) MSDs of the vesicle trajectories after 24 and 48 h of incubation with NPC2 (black symbols) with overlayed fit to the model for anomalous diffusion plus flow (see eqn 5; fit to 24-h data in blue and to 48-h data in red with 95% confidence interval of the regression in green). This model provides the anomalous diffusion constant (B) and the velocity of the vesicles (C). After segmentation of the trajectories into a population where vesicles move by confined diffusion versus normal diffusion + directed motion, the diffusion constant (D) and velocity (E) were determined for the directed population. The inset in (A) shows the fit to a model with Brownian motion only, which, despite smaller parameter confidence intervals, clearly deviates from the experimental data.

calculation is based on a triangulation process and further discussed in Appendix S1 and Figure S4.

Finally, SpatTrack contains the option to analyze particle distributions based on the RDF (59). Here, the number of particles in a range of distances is calculated for each tracked particle and compared to a random distribution.

us, the RDF method may reveal accumulation, repulsion or randomness on longer length scales than the NN approach. For a distribution of N particles, the average number of particles within a distance, r , from particle, p , is given by

$$\langle F(r) \rangle = \frac{1}{N} \sum_{i=1}^N \sum_{k=0}^{R_{\max}} p_i(k\Delta r), \quad (13)$$

where Δr is an increment of the distance by 0.5 pixel multiplied by the pixel size (here $0.222 \mu\text{m}/\text{pixel}$ giving $\Delta r = 0.111 \mu\text{m}$), R_{\max} is the maximal distance of the measurement (in μm), and the triangular brackets denote the average over the number of particles. Using this expression, we de ne $g(r)$, the RDF, as the average number of observed particles within distance, r , divided by the average number of particles within the same distance of a given particle drawn from a random particle distribution (59):

$$g(r) = \frac{\langle F_{\text{obs}}(r) \rangle}{\langle F_{\text{rand}}(r) \rangle}, \quad (14)$$

Here, $\langle F_{\text{obs}}(r) \rangle$ and $\langle F_{\text{rand}}(r) \rangle$ are the average number of particles as a function of distance for the observed and simulated particle distributions, respectively. From this, it is evident that $g(r) = 1$ for a random particle distribution, while $g(r) < 1$ and $g(r) > 1$ indicate repulsion and clustering, respectively. At distances where no other particles are found near the reference particle, $g(r)$ is equal to zero. As described for the other spatial functions, the con dence interval increases with the number of sampled random distributions. us, for n Monte Carlo simulations the average RDF is given by

$$\overline{g(r)} = \frac{1}{n} \sum_{j=1}^n \frac{\langle F_{\text{obs}}(r) \rangle_j}{\langle F_{\text{rand}}(r) \rangle_j}, \quad (15)$$

where $\langle F_{\text{rand}}(r) \rangle_j$ is the number of particles as a function of radius for the j th uniformly random distribution averaged over the total number of particles. e bar denotes averaging over the number of Monte Carlo simulations. e add-on for RDF analysis is shown in the upper panel of

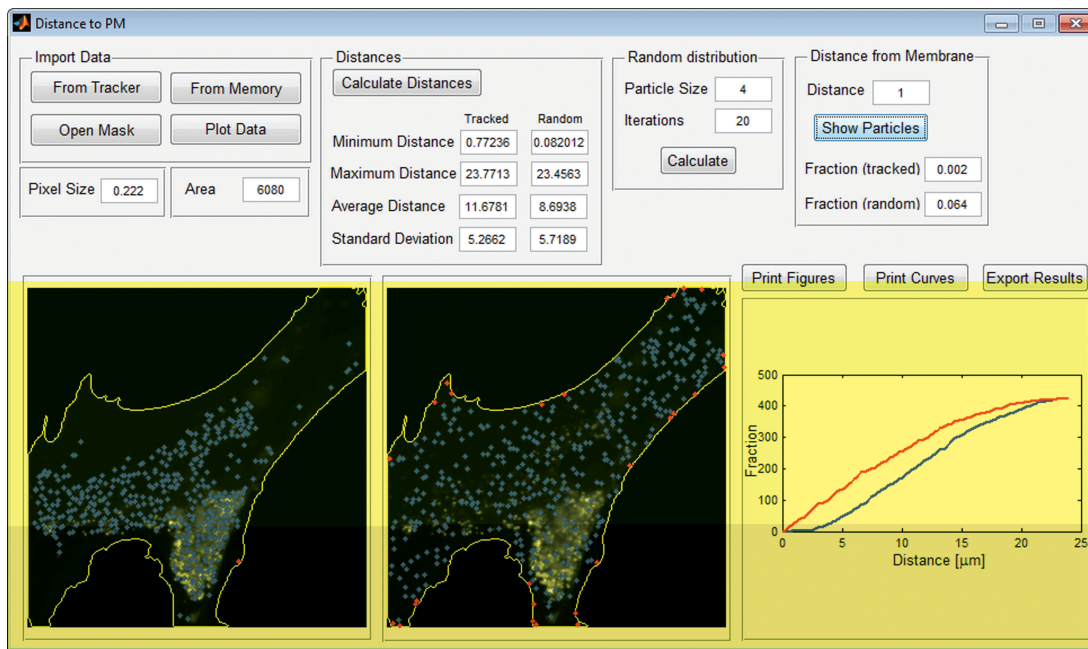


Figure 4: GUI for determining particle's distance to the PM. The distance between tracked particles and the PM is one measure of the particles' spatial distribution. The GUI developed for that purpose compares the spatial distribution of the tracked particles (left image) to a random distribution of the same number of particles in the same geometry (middle image). The blue and red dots show the particles with a distance of more than and less than 1 μm to the PM, respectively. In this example, only one of the tracked particles was found within 1 μm to the PM. In the plot to the right, the red and blue curves show the number of particles within a given distance from the PM for the random and tracked particle distributions, respectively.

Figure S3B with distribution of tracked vesicles (left) and of random points (right) being visualized in the cell geometry.

Using these tools, we performed a detailed SPA of fluorescent NPC2 in LE/LYSs after incubating cells for 24, 48 and 96 h with the protein. First, we calculated the average number of LE/LYSs containing fluorescent NPC2 and the average cellular area as a function of incubation time from 15 cells at each time-point. This clearly showed that both the number of LE/LYSs and the cellular area increase over time (Figure 5A,B). Interestingly, the fractional area occupied by LE/LYSs with respect to the total cell area remained stable at $\sim 60\%$ at all time-points, see Figure 5C.

The increased area is most likely a consequence of the cells becoming more flat over time. Cell flattening might be a direct consequence of NPC2-mediated sterol eflux or caused by the prolonged incubation of cells for several days without sub-cultivation to new growth areas (i.e. primary fibroblasts tend to organize in a skin-like layer over time). We calculated the ANN, as described in eqn 11, using the

add-on to SpatTrack presented in Figure S3A. To give a confidence interval of 95%, the distribution of tracked particles was compared to 20 randomly generated point distributions. For each iteration of this simulation, the ANN was calculated, and the final ANN was then expressed as the average of the ANN from each iteration. This calculation was performed for 15 cells and the result was averaged for each condition (Figure 5D). From this analysis, one can infer a random distribution of NPC2-containing vesicles at the spatial scale of the NN measure, indicating that their position is independent of each other (see above, and eqns 11 and 12). The number of LE/LYSs as a function of the distance to the PM was next calculated for each cell, and the result was averaged for each time-point (Figure 5E). Here, the number of NPC2 positive vesicles is given as a function of their distance from the PM for 24, 48 and 96 h of incubation in black, blue and red, respectively. Clearly, NPC2 is located closer to the PM at later time-points of cholesterol eflux. To see if this coincides with any particle clustering or dispersion over longer length scales,

we determined the RDF for NPC2-containing vesicles in fibroblasts at the different times of incubation. Note, that, like the NN analysis, this measure is independent of the total number of vesicles, as it is expressed as a ratio with the random population in the denominator (see $\overline{g(r)}$ in Figure 5F and eqns 14 and 15). Again, $\overline{g(r)} = 1$ indicates a random distribution, while $\overline{g(r)} < 1$ and $\overline{g(r)} > 1$ indicate repulsion and accumulation, respectively. The analysis shows that for distances smaller than $\sim 1.7 \mu\text{m}$, the LE/LYSs are randomly distributed, while they tend to cluster on longer length scales (Figure 5F). Interestingly, the degree of accumulation decreases with incubation time, which is consistent with a more scattered distribution of NPC2 on longer length scales over the course of cholesterol efflux. More scattered and mobile vesicles closer to the PM could contribute to exocytosis of some NPC2 protein, as recently suggested for lysosomal cholesterol egress occurring via fusion of sterol-rich lysosome-derived vesicles with the PM (60).

NPC2 is only little targeted to sterol-rich LSOs

Based on these findings, we were interested in determining the spatial relationship between the NPC2-containing vesicles and the cholesterol-rich LSOs. During continuous incubation with Alexa546-NPC2, the fluorescence of lipin decreased gradually, while that of NPC2 increased (Figure S5A). By visual inspection of the images, a noticeable aspect is the very low colocalization of Alexa546-NPC2 with lipin during cholesterol efflux (see inset in Figure S5B–D). With increasing incubation time, fluorescent NPC2 becomes enriched in vesicles that often are in close contact to the lipin-positive LSOs. For colocalization analysis, the images were first denoised in both channels using SpatTrack, and subsequently pixels with an intensity lower than eight times the average intensity of the image were set to zero (see Figure 5E–G). Several different measures of colocalization between the signal in two channels exist, see for example (22). Two commonly used measures are Pearson's correlation coefficient (PCC) and Mander's overlap coefficient (MOC; see definition in Appendix S1). Both parameters were calculated using the JACoP plugin for ImageJ (22) from images of lipin- and Alexa546-NPC2-stained cells after 24, 48 or 72 h of incubation (Figure S4E,F). The PCC was ~ 0.2 at all time-points, suggesting a weak colocalization between lipin and Alexa546-NPC2. In contrast,

the MOC for both fluorophores increased with incubation time, indicating that after 72 h of incubation, a larger fraction of pixels in both channels were overlapping. While both PCC and MOC provide a measure for the degree of colocalization between two fluorescently labeled molecules, they are both pixel-based methods. This means that PCC and MOC do not provide information about the objects to which the colocalizing molecules belong. To determine which vesicles are colocalized, we implemented a particle-detection-based colocalization analysis (PDBCA) into SpatTrack (Figure 6). Object- or particle-based assessment of colocalization has been used by several groups for a variety of problems in the past, ranging from quantification of colocalizing membrane proteins (61,62) over assessment of endosome distribution in the developing fruit fly (63) to endocytic sorting in mammalian cells (23). Detecting which particles are colocalized may be considered as a variation of the NN linking scheme used in SPT (29,64). However, rather than linking particles in time, in PDBCA, particles detected in one channel are linked to particles detected in the other channel. After particle detection by SpatTrack in both channels, the diameter of each particle is determined by fitting a 2D Gaussian to the denoised image in a square area large enough to contain the particle but so small that the other particles are excluded (Figure 6B). Finally, the average of the two median sizes, M , is used for further analysis, and as criterion for colocalization, a value of 0.5 times M is chosen (typical values for M are 200–500 nm; Figure 6C). For the data presented here, we would often find a different number of particles in each channel (i.e. in the lipin and NPC2 channels). Therefore, to avoid linking one particle in one frame to multiple particles in the other, we choose the population containing fewer particles as the reference and consider the other population as candidate particles, as suggested previously (61,62). Then, for each reference particle, the distance to the nearest candidate particle is determined, and particles which are closer to each other than M times a scaling factor are considered to be colocalized (see flowchart in Figure 6A).

We performed the PDBCA analysis on the same data set as used for calculating PCC and MOC (see above and Figure S5). Per cell, the algorithm detected about 720 and 745 particles containing lipin and Alexa546-NPC2,

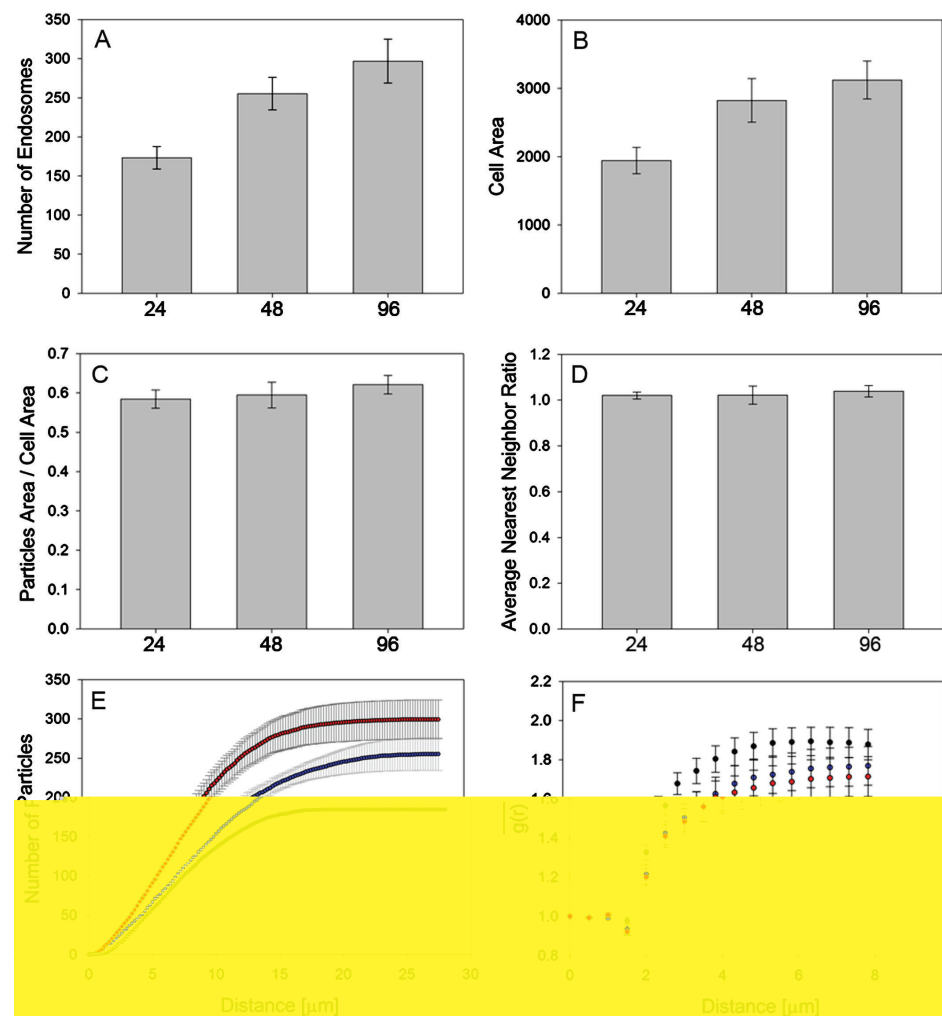


Figure 5: SPA of NPC2-containing vesicles in disease fibroblasts. NPC2 disease fibroblasts were cultured in medium containing LDL and other lipoprotein sources before switching to medium containing LPDS and 100 nm Alexa488-NPC2 for 24, 48 or 72 h. Cells were washed and imaged on a widefield microscope. The SPA in SpatTrack revealed that both, the number of NPC2-containing vesicles (A) and the cell size (B), increase over time when the cells are incubated with Alexa488-NPC2. Further analysis showed that the fraction of the cell occupied by vesicles is approximately constant over time (C) and that, at all time-points, the vesicles are randomly distributed on the NN length scale (D). E) a plot of the number of NPC2-containing vesicles as a function of the distance to the PM for 24 h (black symbols), 48 h (blue symbols) and 96 h (red symbols) of incubation with the protein. Finally, (F) shows the analysis by the RDF for each time-point in the same colors as used in (E). This analysis shows that the vesicles are accumulated compared to a random distribution but less so with increasing incubation time.

respectively. Between 10 and 20% of the LE/LYSs containing Alexa546-NPC2 overlapped with LSOs stained with 1-lipin at all time-points (Figure 6H). However, there was a higher degree of colocalization after 72 and 96 h of incubation than after 24 and 48 h. On average, each cell contained 80 ± 11 colocalizing vesicles, which we deemed too few to perform a meaningful pattern analysis. However,

visual inspection of the spatial location of the colocalized endosomes suggested that they were randomly distributed in the cell.

Two-color SPA

Having the coordinates of both vesicle populations from the PDBCA, we went on to determine colocalization and

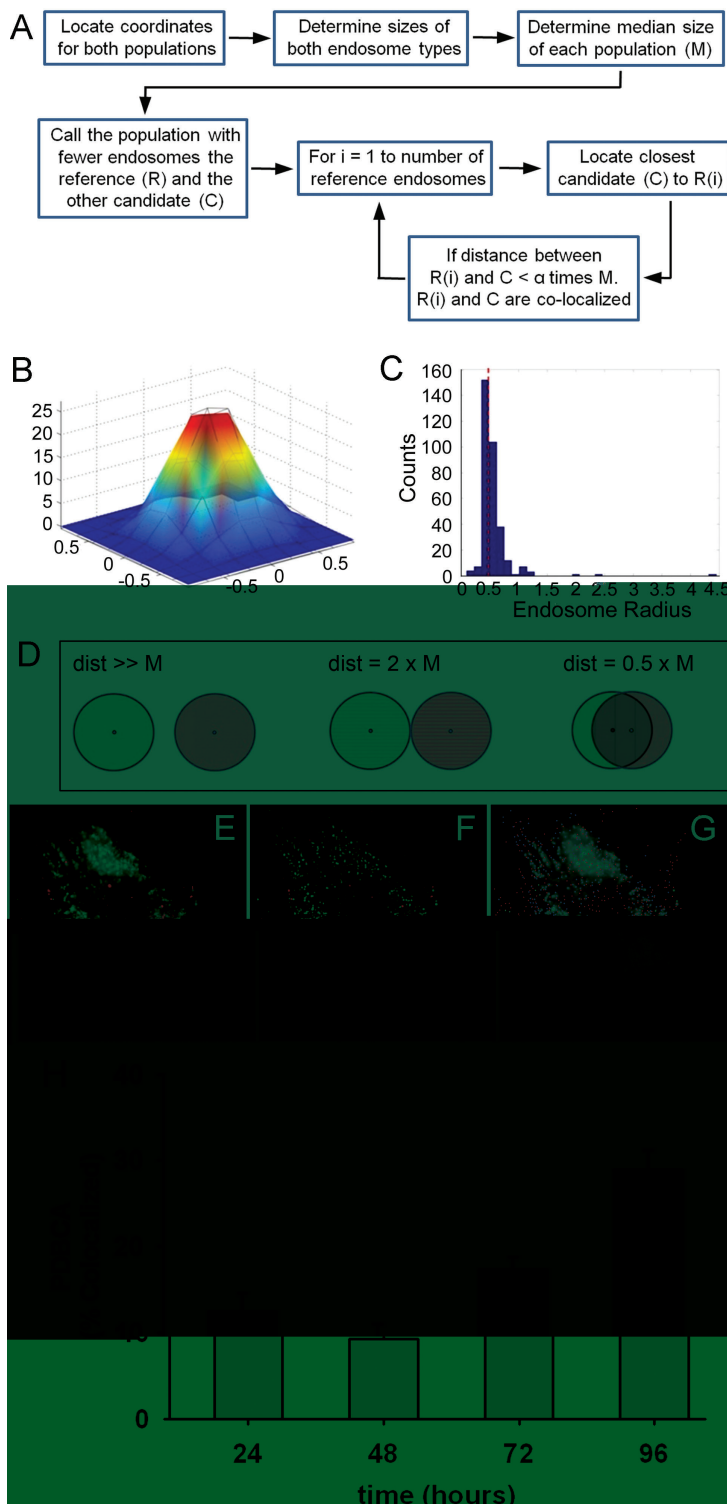


Figure 6: PDBCA of Alexa546-NPC2 versus filipin. The workflow of PDBCA is shown in (A). First, the images are denoised using the boxcar filter after which the median size of both particle populations is determined by fitting a 2D Gaussian to each particle in each channel (B and C). Then particles closer to each other than a scaling factor times the median particle size are considered to be colocalized. D) Examples of three different scaling factors. For the analysis presented here, we chose a value of $dist = 0.5$ as criterion for particle colocalization corresponding to 84% particle overlap. NPC2 disease fibroblasts were labeled as described in *Materials and Methods*, and colocalization was assessed using the PDBCA routine implemented in SpatTrack. A color overlay with filipin in green and Alexa546-NPC2 in red is shown prior to (E) and after denoising (F). After performing the PDBCA, the program highlights vesicles containing only filipin and Alexa546-NPC2 in blue and red, respectively, while vesicles with both markers being judged as colocalized are labeled in yellow (G). The fraction of colocalized vesicles as determined by the PDBCA for various incubation times with fluorescent NPC2 and with filipin as reference channel. Using Alexa546-NPC2 as reference gave comparable results (not shown). The data represent mean \pm SE of at least six images with 2–4 cells per condition.

eventual spatial relationships between Alexa546-NPC2 and filipin by two-color SPA. This approach, as shown in the following section, provides additional information about possible particle interaction and provides an independent

measure of colocalization. SPA is scale dependent, as illustrated in Figure 7A: if we consider the distribution of red and green particles in the dashed box, they appear to be mutually repulsive. However, if we consider the two types

of particles on a larger length scale (i.e. in the full box), the two particle populations appear to accumulate in clusters. To account for this, we developed a two-color RDF analysis method that considers the average number of particles from one population within a given distance of a particle from the other population. If we define $N_{12}(r)$ as the number of particles of type 2 within a distance r from a particle of type 1, then the average $\langle N_{12}(r) \rangle$ for a population of N_1 particles of type 1 is given by

$$\langle F_{12}(r) \rangle = \frac{1}{N_1} \sum_{i=1}^{N_1} \sum_{k=0}^{R_{\max}} N_{12}^{P_{1,i}}(k\Delta r), \quad (16)$$

Here, Δr is a size increment, R_{\max} is the maximal distance entering the measurement, $N_{12}^{P_{1,i}}$ is the number of particles of type 2 as a function of the distance to the i th particle of type 1 and the triangular brackets denote averaging over the number of type 1 particles. From this we define the RDF for type 1 particles with respect to particles of type 2 as follows:

$$g_{12}(r) = \frac{\langle F_{12}^{\text{obs}}(r) \rangle}{\langle F_{12}^{\text{rand}}(r) \rangle}, \quad (17)$$

Here, the indices ‘obs’ and ‘rand’ refer to the observed and simulated particle distribution in the cell geometry, as described above for the one-color RDF (eqns 13–15).

us, $\langle F_{12}^{\text{rand}}(r) \rangle$ gives the average number of particles from a uniformly sampled random distribution of particles containing the same number of particles as population 2 within a distance r from a particle of type 1. Accordingly, if the particles in populations 1 and 2 are randomly distributed with respect to each other, one gets $g_{12}(r) = 1$, while for mutual accumulation or repulsion, the result will be $g_{12}(r) > 1$ or $g_{12}(r) < 1$, respectively. The statistical significance of the measure may be increased by comparing the observed particle distribution to an increasing sample of random populations. us, for a comparison with n random distributions, the two-color RDF for population 1 with respect to population 2 is given by

$$\overline{g_{12}(r)} = \frac{1}{n} \sum_{i=1}^n \frac{\langle F_{12}^{\text{obs}}(r) \rangle}{\langle F_{12}^{\text{rand}}(r) \rangle_i}, \quad (18)$$

Here $\langle F_{12}^{\text{rand}}(r) \rangle_i$ is the average number of particles from population 2 as a function of distance to a particle in population 1, and the bar indicates averaging over n simulations.

In Figure 7C, an example of a NPC2 disease broblast after 24 h of incubation with Alexa546-NPC2 and staining of free cholesterol with lipin is shown. Here, blue and red dots indicate the positions of detected particles in the lipin and Alexa546-NPC2 channel, respectively. Although most particles are not colocalized, they are primarily located in the same area of the cell. To analyze this further, we calculated the two-color RDF for each vesicle population with respect to the other, as shown for the particular cell in Figure 6B (blue and red symbols give the number of NPC2-containing LE/LYSs as a function of distance to the lipin containing LSOs and vice versa). In addition, the curves for the number of randomly distributed particles for each condition are shown as blue and red dashed lines, respectively. Clearly, the mutual distance of LE/LYSs labeled with Alexa546-NPC2 and LSOs stained with lipin is lower for a given number of particles than for a random distribution for all inter-particle distances between 0.15 and 5 μm (Figure 7B). This confirms the visual impression that both vesicle populations appear to be clustered in the perinuclear area of the cells. The two-color RDF was calculated for this cell, in which each population of vesicles was compared to 20 populations of randomly distributed particles. That is, 20 runs of the Monte Carlo simulation were performed to generate independent and randomly distributed vesicle patterns in the cell geometry from which the function $F_{12}(r)$ was calculated according to eqn 16. Subsequently, this entered the calculation of the two-color RDF, $\bar{g}(r)$, evaluated for both vesicle populations according to eqn 18 (Figure 7D; the indices were omitted for the sake of brevity). It can be seen that the value of $\bar{g}(r)$ is between 12 and 22 for inter-particle distances, $0.1 \leq r \leq 0.15 \mu\text{m}$, while it drops sharply for larger distances. For longer distances, this measure declines steadily with a value of $\bar{g}(r) \sim 1.8$ at $r = 4 \mu\text{m}$ (Figure 7D). Finally, we performed the same calculation for all image data of lipin versus Alexa546-NPC2 at the respective time-points of cholesterol efflux (Figure 7E). For that purpose, the two-color RDF between lipin as population 1 and Alexa546-NPC2 as population 2 was calculated for the complete data set as used for the colocalization based on the PCC and MOC and for the PDBCA, above (compare Figure 6 and S5). We find again an increasing peak in the two-color RDF for distances up to $\sim 0.11 \mu\text{m}$ over the time course of incubation with Alexa546-NPC2. This peak at $r = 0.11 \mu\text{m}$ resembles the half mean diameter

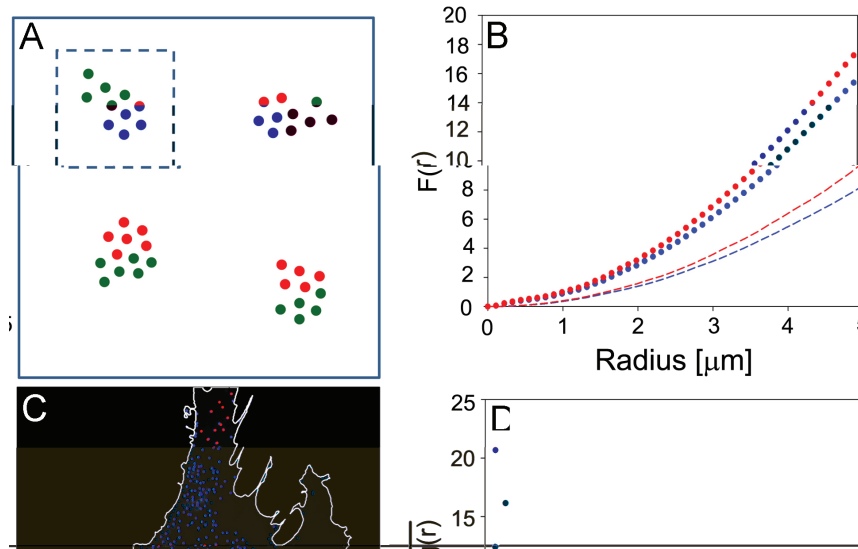


Figure 7: Two-color RDF for Alexa 546-NPC2 versus filipin. A) How the SPA is scale dependent is illustrated: vesicles in red and green appear to be clustered in four groups on a large scale, while they are clearly segregated on a smaller scale (indicated by the dashed box). The red- and blue-dotted curves in (B) show this with the red or blue population as reference, respectively. The dashed curves in (B) show the result for a randomly placed particle population. C) The distribution of two particle populations in a cell from which the two-color RDF analysis was performed is shown. For the red distribution, the average number of blue particles is determined as a function of radius and vice versa. Finally, the red and blue curves in (D) show the ratio between the observed and random curves of (C). For this example, the observed populations were compared against 20 random populations giving a confidence interval of $\pm 5\%$. E) The two-color RDFs were calculated according to eqn 18 for all cells at a given incubation time in LPDS with 100 nm Alexa546-NPC2 (i.e. brown, orange, light green and dark green symbols correspond to 24, 48, 72 and 96 h of incubation, respectively). The inset shows the two-color RDFs for radii of up to 1.5 μm . The data represent mean \pm SE of at least six images with 2–4 cells per condition. A second experiment gave comparable results (not shown).

of the particles estimated from the Gaussian fit to particle sizes (i.e. M in Figure 6D; see also above). In us, this peak in the two-color RDF represents colocalization of the average-sized vesicles in the total population. We suggest that the concurrent calculation of the two-color RDF and the PDBCA, both implemented in SpatTrack, provide a new unbiased method for judging colocalization of spherical particles in living cells, irrespective of the time of incubation with Alexa546-NPC2. A t(v)-3.94(inc1(d)-541.3(f)54.1(d)-7.20003 TAlexa5,7-3340 -12i)080Tf n the.1(d45-13.2(p)-51

Alexa546-NPC2-containing LE/LYSs after 72 and 96 h compared with 24 and 48 h of incubation with NPC2. This trend was also found in the PDBCA shown in Figure 5H, confirming that both methods provide complementary information. From the shoulder peaks of declining height in the two-color RDF, one can additionally conclude that both vesicle populations appear to cluster at distinct distances of $r \sim 0.25$ for all times of cholesterol efflux (Figure 7E). This could be a consequence of the particular packing geometry of the vesicles relative to the nucleus and/or of interactions of vesicles with the cytoskeleton being oriented in specific geometries in the cells.

Discussion

In this study, we have presented a new software suite as a tool for in-depth analysis of endosomes and other point-like objects in living cells. SpatTrack collects a variety of algorithms for detailed analysis of vesicle motility and movement types, spatial distribution and content of several cargos. It can be used in batch processing mode allowing for execution of repeated image processing tasks without user intervention. Details of the program are described in a user guide to SpatTrack and are available in Appendix S1. Using these tools, we show for the first time, that internalized NPC2 is efficiently removing the aberrant cholesterol accumulations from NPC2 disease cells, while it accesses only a subpopulation of the sterol-storage compartments. We demonstrate that NPC2-mediated cholesterol efflux is accompanied by increasing motility and scattering of the NPC2-containing vesicles. We propose that the lysosomal cholesterol stores are sub-compartmentalized into different vesicle populations of which only a minor portion is accessible for incoming endocytic cargo. In support of this notion, we found that the bulk endocytosis marker dextran has only very limited access to the lipid-positive vesicles in NPC2 disease fibroblasts (not shown).

The analysis tools implemented in SpatTrack can serve a wide variety of purposes in cell biology. The range of other applications starts at determining the dynamics and spatial distribution of other endocytic cargo along the lysosomal and endocytic recycling pathway. It has been convincingly demonstrated that the intracellular distribution and dynamics of endocytic vesicles is related to their function. In particular in NPC disease fibroblasts,

misrouting of endocytic cargo to aberrant LE/LYSs is a prominent part of the disease phenotype, as shown for the recycling marker transferrin and for various glycoproteins (65,66). The endocytic sorting capacity of fibroblasts can be assessed with high spatiotemporal accuracy using SpatTrack. Small GTPases, like rab7, are involved in lysosomal targeting of LDL and other cargo, and dominant-negative rab7 was not only unable to mediate LDL degradation but also incapable of ensuring correct positioning of the late endocytic compartments carrying this lipoprotein (67). Many other proteins are involved in late endosome positioning in mammalian cells, like the cholesterol sensor ORPL1 (68). Using live-cell imaging with SpatTrack for image analysis combined with RNA interference, the function of these proteins could be studied in detail and with high reliability. High statistical accuracy of vesicle quantification is also a precondition for accurate modeling of cargo tracking along the endocytic pathway, as, for example, set about in 11, 57, 69). Second, SpatTrack can be combined with ratio imaging to measure the pH, calcium or chloride content of endocytic and lysosomal vesicles in dependence of the exact location of the vesicles in the cells (4). Third, SpatTrack might be useful to follow the course of induction of autophagy. Here, the local enrichment of the autophagosomal marker Atgl8 tagged with eGFP is often taken as evidence for autophagosome formation over time (70). Long-term tracking of photoactivatable eGFP-tagged Atgl (PA-eGFP-Atgl8) has been used to determine the turnover time of autophagosomes (71), and this analysis could be simplified and automatized by SpatTrack. Fourth, the biogenesis of lipid droplets, their positioning and marker content, e.g. after cellular loading with fatty acids or cholesterol or under starvation conditions, can be studied using SpatTrack (49,72). Fifth, the dynamics of assembly and disassembly of inclusion bodies, as found in several neurodegenerative disease, as Huntington disease can be studied using SpatTrack, thereby supplementing other approaches, as fluorescence recovery after photobleaching (FRAP) or fluorescence loss in photobleaching (FLIP) (73,74). As SpatTrack is a tool for 2D analysis of particle patterns and dynamics, applications with thin cells should be preferred. SpatTrack can also be of use in determining colocalization, clustering and distribution modes of protein assemblies in the PM, for example, of clathrin coated pits or membrane receptors (75,76). Finally, SpatTrack might also supplement

current approaches for analysis of protein clustering by superresolution microscopy (63,77).

Materials and Methods

Reagents

Succimidyl ester of either Alexa647 dye (emission in infrared), of Alexa546 dye (emission in red) or of Alexa488 dye (emission in green) were purchased from Invitrogen/Molecular Probes Inc. Filipin, paraformaldehyde (PFA) and rhodamine–dextran were from Sigma Aldrich. Buffer medium contained 150 mM NaCl, 5 mM KCl, 1 mM CaCl₂, 1 mM MgCl₂, 5 mM glucose and 20 mM HEPES (pH 7.4).

Protein purification and labeling

Purification of NPC2 was performed as described by Larsen and co-workers (78). The identity and purity of the recovered protein was confirmed by SDS-PAGE analysis in 16% Tris/Tricine gels followed by Coomassie brilliant blue staining and N-terminal amino acid sequencing carried out by automated Edman degradation (Procise Protein Sequence Model 491; Applied Biosystems). No additional bands or sequences besides NPC2 were detected. On average approximately 3 mg of the highly purified bovine NPC2 were extracted per liter of milk as determined by acid hydrolysis followed by quantitative amino acid analysis. NPC2 was subsequently labeled with either Alexa Fluor 488 (yielding Alexa488-NPC2) or Alexa Fluor 546 (yielding Alexa546-NPC2) protein labeling kits as instructed by the manufacturer (Microscale Protein Labeling Kit, Invitrogen Inc.). The labeled proteins were analyzed by SDS-PAGE and visualized using a Typhoon Trio fluorescence scanner (GE Healthcare). In addition, absorption spectrometry was used to estimate the labeling ratio as suggested by the manufacturer.

Staining of cellular cholesterol with Filipin

Fibroblasts were seeded on microscope dishes with glass cover slips inlet and settled for 24 h. Cells were cultured in medium containing LPDS in the absence or presence of 100 nM NPC2 or Alexa546-NPC2 for 48 h, washed in ice-cold buffer medium and stained with filipin as described (79). Briefly, the cells were fixed with 3% PFA in PBS for 1 h at room temperature, washed and quenched with 50 mM glycine in PBS. Cells were then incubated for 2 h at room temperature in buffer medium containing 50 µg/mL filipin added from a stock solution in DMSO (final concentration 0.2% v/v). After the incubation, filipin was removed by rinsing the cells several times with buffer medium. Cells were imaged as described below.

Cell Culture and incubation with fluorescent NPC2

NPC2 deficient human skin fibroblasts (from Coriell Institute #GM18455) were grown at 37°C in an atmosphere of 5% CO₂ until 90% confluence in complete DMEM culture medium supplemented with 1% glutamine, 1% penicillin and 10% FBS. The cells were placed on microscopy dishes and allowed to settle for another 48 h in the same growth medium during which time they accumulated additional cholesterol in the LSO

by continuous uptake of LDL. Subsequently, the cells were incubated with 100 nM Alexa488- or Alexa546-labeled NPC2 protein in growth medium where FBS was exchanged for 10% LPDS, a lipoprotein-depleted serum lacking all potential cholesterol carriers. Cells were washed with buffer medium immediately before imaging, and images were acquired as described below.

Microscopy

Images for mobility analysis of LE/LYSs containing fluorescent NPC2 were acquired on a motorized, inverted Nikon Ti-E microscope with Perfect Focus Control coupled to a Yokogawa CSU-X1 spinning disc confocal system and equipped with a 60× oil immersion objective (NA = 1.4) and an Andor Laser launcher with 405, 491, 514, and 561 nm laser lines as illumination sources. For excitation of Alexa546-NPC2, the 561 nm laser line was used. This microscope has an electron-multiplied CCD camera (Andor EMCCD DU-885, 1004 × 1002 pixels, 8 × 8 µm) as detector. Each image sequence contained 125 frames acquired with a frame rate of 1 Hz. During imaging, the cells were kept in an Okolab microscope stage incubator providing a temperature of 37°C and humidified atmosphere. Wide field epifluorescence microscopy was carried out on a Leica DMRB microscope with a 63 × 1.4 NA oil immersion objective (Leica Lasertechnik GmbH) with a Lambda SC smartshutter (Sutter Instrument Company) as illumination control. Images were acquired either with an Orca 2 CCD camera (Hamamatsu Photonics) or with an Andor Ixon^{EM} blue EMCCD camera operated at -75°C and driven by the SOLIS software supplied with the camera. Filipin was imaged using the Leica A-cube

of each particle within an area determined by the estimated particle size. This procedure is performed for each particle in each image in the stack. Subsequently the program links particles in one image to particles in the next image. Linking is performed by an NN approach, which means that particle movement from one frame to the next must be relatively small. For a thorough description of the tracking algorithm, we refer the reader to the article by Crocker and Grier and our previous publication (29,30). Defining a maximum displacement enhances the speed of the program significantly, since for a given particle only particles within the maximum distance are considered for linking. In addition, the user may choose the minimum trajectory length in frames. For our experiments, we chose to consider only full-length trajectories (i.e. for particles found throughout the whole time-lapse sequence).

Generation of simulated point patterns

Particle patterns were first generated for determining the ANN and RDF of randomly distributed particles relative to the tracked vesicles (see eqns 11 and 12 and eqns 14–18). To this end, a set of x - and y -coordinates are first generated in the intervals $\min(x) < \mathbf{x} < \max(x)$ and $\min(y) < \mathbf{y} < \max(y)$. Here, $\min(x)$, $\min(y)$, $\max(x)$ and $\max(y)$ indicate the minimum and maximum x - and y -coordinates of the cell boundary, and \mathbf{x} and \mathbf{y} are vectors containing the generated coordinates. To ensure a sufficiently large number of coordinates for the following steps, $4n$ random points were generated from a uniform PDF, where n is the number of tracked particles. Subsequently, the points lying outside the cell were discarded.

Calculating the area of the point distribution

In the add-on for NN analysis, it is possible to calculate the area of the tracked particles normalized to the total cell area. Calculation of the cellular area occupied by fluorescent vesicles is implemented in the following way: initially, the detected particles are connected by a Delaunay triangulation where the outer line segments make up the convex hull. For a convex particle distribution, the convex hull will fit tightly around the circumference of the particle cloud, see Figure S4A. However, for concave point distribution, the convex hull does not touch all of the outer particles, leading to an overestimation of the particle area, see Figure S4B. To overcome this problem and to refine the triangulation, we apply an alpha-shape procedure (80,81). First, a circle with radius, $r = \alpha \cdot \langle NN_{obs} \rangle$, is placed on each line segment of the Delaunay triangulation, where $\langle NN_{obs} \rangle$ is the average NN distance of the particle distribution (see green circle in Figure S4B). For each circle, it is determined, whether it contains or touches any of the particle coordinates. Line segments containing empty circles are deleted. Thus, for a sufficiently large radius the alpha shape is identical to the Delaunay triangulation, while for a sufficiently small radius, the alpha shape is empty. In Figure S4C, the alpha shape is shown after the long-edge segments of the triangulation have been removed, while Figure S4D shows the Delaunay triangulation of a set of detected vesicles inside the cell geometry. Here, some line segments stretch outside the cell boundary. As the area made up by the vesicles cannot extend outside the cell geometry, these line segments are deleted prior to the alpha-shape procedure, see

Figure S4E. Finally, the triangulation is refined by alpha shaping, see Figure S4F.

Additional image analysis

To eliminate artificial motion from cell movement, the image stacks were registered using the StackReg plugin for ImageJ (82) prior to tracking in SpatTrack. Filipin intensity measurements and calculations of the fraction of cholesterol stored in the LE/LYSs were determined using an in-house developed plugin for ImageJ.

Computational implementation of SpatTrack

All algorithms were implemented in MatLab as 64-bit Windows version.

The program including a User Guide and sample images for use in combination with the guide is freely available from www.sdu.dk/bmb/spattrack. Running SpatTrack does not require installation of MatLab, but it demands installation of the MatLab compiler runtime (MCR) version 2012a (7.17) available at <http://www.mathworks.se/products/compiler/mcr/>.

Acknowledgments

D. W. acknowledges funding from the Danish research Councils FNU and FSS, the Lundbeck Foundation and the NovoNordisk Foundation. The Danish Microscopy and Bioimaging Center (DaMBIC) is acknowledged for providing access to the spinning disk microscope. The authors declare no conflict of interest.

Supporting Information

Additional Supporting Information may be found in the online version of this article:

Appendix S1: Contains information about the performed Monte Carlo simulations, about estimation of free cholesterol and Alexa488-NPC2 in the LYSs, about SPA, calculation of the area occupied by NPC2-containing endosomes and about the performed pixel-based colocalization analysis.

Figure S1: Validation of the decision tree for MSD analysis. To test the first steps in the decision tree, additional vesicle simulations were performed, in particular of diffusion plus flow and normal/hindered diffusion. MSDs of simulated trajectories of diffusion plus flow with variable diffusion constant and/or velocity were analyzed by the SE of the fitted parameters followed by analysis using the BIC. A and B) The percentage of trajectories correctly classified as diffusion plus flow is shown. Each square represents the analysis of 100 MSDs generated as the ensemble average of 100 trajectories with a length of 100 steps. For trajectories, in which the velocity was small compared with the diffusion constant, decreasing the frame rate from 10 frames/second to 1 frame/second increased the number of correctly classified trajectories. For most parameter combinations, the combined analysis of the parameter's SEs followed by BIC analysis led to a correct classification (i.e. in more than 80% of the analyzed MSDs). In addition, the MSDs of simulated trajectories of Brownian diffusion with different diffusion constants were

analyzed. Here, the procedure described in the decision tree classified 75% of the MSDs as Brownian diffusion or anomalous diffusion (C). For MSDs of short lag times close to 100% of the trajectories classified as anomalous diffusion had an anomalous exponent larger than 0.9, (D) and were, thus, classified as Brownian diffusion.

Figure S2: Function and transport of NPC2 in disease broblasts. Filipin intensity and distribution in cells after 0 and 48 h of growth in LPDS without NPC2, (A) and (B), respectively, and after 48 h of growth in LDPS with 100 nM NPC2 (C). D) The fraction of lipin in the LSO with respect to the total cellular lipin at the three different conditions is shown. Filipin is a marker for free cholesterol. Thus, (D) shows that after 48 h of growth without NPC2 ~34% cholesterol is exposed, while 65% cholesterol is exposed over 48 h in the presence of functional NPC2. Data represent mean \pm SEM of two separate experiments with each having recorded at least five fields having 1–3 cells per field and condition. Fluorescent NPC2 is targeted to LSOs and recycles slowly to the cell surface. E,F) Uptake of NPC2. NPC2 disease broblasts were incubated overnight with 0.5 mg/mL Rh-Dextran to prelabel LSOs. Cells were subsequently incubated with 100 nM Alexa488-NPC2 in LPDS containing medium for the indicated time-points (72 h in E). Fluorescence of Alexa488-NPC2 in the LSOs was quantified as described in *Materials and Methods* and plotted as function of time (F, symbols, mean \pm SE; $n = 30$). The data were fitted to a mono-exponential function without residual (F, green line). After 48 h of uptake as described above, cells were switched to medium containing LPDS but no NPC2 protein and kept there for the indicated time-points. Fluorescence of Alexa488-NPC2 in the LSOs was quantified as described above (G, symbols, mean \pm SE; $n = 16$) and fitted to a mono-exponential decay function with residual. On average, 3–6 cells were imaged per field giving the indicated number of images, i.e. n , per time-point. Bar, 10 μ m.

Figure S3: GUI for determining nearest neighbors (NN; A) and the RDF (B). The histograms of NN distances are placed under the cell images for the tracked (A, lower left bar plot) and simulated particle distribution (A, lower right bar plot), respectively. In the RDF analysis (B), the number of particles within a distance from a reference particle is compared to the same measure for the random particles. This yields a function $\langle F(r) \rangle$, as defined in eqn 13, for the tracked and random particle distribution (black and blue symbols in the lower left plot of (B)). The ratio of measured and simulated $\langle F(r) \rangle$ gives a function $g(r)$ according to eqns 10 and 11 with $g(r) = 1$ for a random distribution and $g(r) < 1$ or $g(r) > 1$ for a repulsive or aggregating particle population, respectively. For the particle population examined here, it can be seen that $g(r) \sim 1$ for distance of less than ~2 μ m and $g(r) \sim 1.6$ for distances of more than 4 μ m, indicating vesicle aggregation over longer distances. The spatial distribution of the tracked and simulated particles is shown in the cell geometry in the central left and right images of (A) and (B), respectively.

Figure S4: Illustration of the triangulation process. A theoretical example is shown in (A–C), while the result on a set of detected endosomes inside a cell is shown in (D–F). First, the Delaunay triangulation is calculated for the particles. The outer rim of the triangulation is the convex hull that fits tightly around a convex particle distribution (A). However, for a concave particle distribution, the convex hull overestimates the particle area (B). Next, the triangulation is refined by alpha shaping. A circle with radius α is placed on each line segment (green circle in (B)) and line segments where the circle does not contain any particles are deleted. C) The area after alpha shaping is shown. In (D),

the Delaunay triangulation is shown for a distribution of endosomes inside a NPC2^{-/-} cell. Initially, line segments crossing the cell boundary are deleted as the area occupied by the endosomes cannot extend the cell geometry, compare (D) and (E). Next, the alpha-shape procedure is applied to generate the final triangulation (F). The procedure allows for calculating the fractional area occupied by the particles.

Figure S5: Pixel-based colocalization analyses of Alexa546-NPC2 and lipin. NPC2 disease broblasts were cultured in medium containing LDL and other lipoprotein sources before switching to medium containing LPDS and 100 nM Alexa546-NPC2 for either 24, 48 or 72 h. Cells were washed, fixed with PFA and stained for free cholesterol using the polyene lipin as described in *Materials and Methods*. Images were pseudo-colored using an appropriate LUT in ImageJ with lipin in green and Alexa546-NPC2 in red. A) A linear LUT shows the relative intensities for lipin and Alexa546-NPC2 (i.e. decreasing and increasing over time, respectively). Bar, 20 μ m. B–D) the same fields with enhanced contrast to highlight the low extend of colocalization between NPC2 and sterol (see also insets in B–D) is shown. E) Pearson colocalization coefficient ('PCC') and (F) Mander's overlap coefficient ('Manders') calculated between the NPC2 and lipin channel after image denoising from 13 images at each time-point, and the bar plots are displayed with error bars of ± 1 SE.

References

- Geuze HJ, Slot JW, Schwartz AL. Membranes of sorting organelles display lateral heterogeneity in receptor distribution. *J Cell Biol* 1987;104:1715–1723.
- Stoorvogel W, Strous GJ, Geuze HJ, Oorschot V, Schwartz AL. Late endosomes derive from early endosomes by maturation. *Cell* 1991;65:417–427.
- Sonawane ND, Thiagarajah JR, Verkman AS. Chloride concentration in endosomes measured using a ratioable fluorescent Cl⁻ indicator. *J Biol Chem* 2002;277:5506–5513.
- Dunn KW, Maxfield FR. Ratio imaging instrumentation. *Methods Cell Biol* 2003;72:389–413.
- Maxfield FR, McGraw TE. Endocytic recycling. *Nat Rev Mol Cell Biol* 2004;5:121–132.
- Sandvig K, van Deurs B. Entry of ricin and Shiga toxin into cells: molecular mechanisms and medical perspectives. *EMBO J* 2000;19:5943–5950.
- Goldstein JL, Brown MS. The LDL receptor. *Arterioscler Thromb Vasc Biol* 2009;29:431–438.
- Storch J, Niemann-Pick C2 (NPC2) and intracellular cholesterol trafficking. *Biochim Biophys Acta* 2009;1791:671–678.
- Dunn KW, McGraw TE, Maxfield FR. Iterative fractionation of recycling receptors from lysosomally destined ligands in an early sorting endosome. *J Cell Biol* 1989;109:3303–3314.
- Mayor S, Presley JF, Maxfield FR. Sorting of membrane components from endosomes and subsequent recycling to the cell surface occurs by a bulk flow process. *J Cell Biol* 1993;121:1257–1269.
- Ghosh RN, Maxfield FR. Evidence for nonvectorial, retrograde transferrin trafficking in the early endosomes of HEp2 cells. *J Cell Biol* 1995;128:549–561.

12. Yamashiro DJ, Maxfield FR. Kinetics of endosome acidification in mutant and wild-type Chinese hamster ovary cells. *J Cell Biol* 1987;105:2713–2721.
13. Hirschberg K, Miller CM, Ellenberg J, Presley JF, Siggia ED, Phair RD, Lippincott-Schwartz J. Kinetic analysis of secretory protein traffic and characterization of golgi to plasma membrane transport intermediates in living cells. *J Cell Biol* 1998;143:1485–1503.
14. Keller P, Toomre D, Díaz E, White J, Simons K. Multicolour imaging of post-Golgi sorting and trafficking in live cells. *Nat Cell Biol* 2001;3:140–149.
15. White J, Johannes L, Mallard F, Girod A, Grill S, Reinsch S, Keller P, Tzschaschel B, Echard A, Goud B, Stelzer EH. Rab6 coordinates a novel Golgi to ER retrograde transport pathway in live cells. *J Cell Biol* 1999;147:743–760.
16. White J, Keller P, Stelzer EH. Spatial partitioning of secretory cargo from Golgi resident proteins in live cells. *BMC Cell Biol* 2001;2:19.
17. Sage D, Neumann FR, Hediger F, Gasser SM, Unser M. Automatic tracking of individual fluorescence particles: application to the study of chromosome dynamics. *IEEE Trans Image Process* 2005;14:1372–1383.
18. Sbalzarini IF, Koumoutsakos P. Feature point tracking and trajectory analysis for video imaging in cell biology. *J Struct Biol* 2005;151:182–195.
19. Sergé A, Bertiaux N, Rigneault H, Marguet D. Dynamic multiple-target tracing to probe spatiotemporal cartography of cell membranes. *Nat Methods* 2008;5:687–694.
20. Helmuth J, Paul G, Sbalzarini IF. Beyond co-localization: inferring spatial interactions between sub-cellular structures from microscopy images. *BMC Bioinform* 2010;11:372.
21. Shivanandan A, Radenovic A, Sbalzarini IF. MosaiciA: an ImageJ/Fiji plugin for spatial pattern and interaction analysis. *BMC Bioinform* 2013;14:349.
22. Bolte S, Cordelières FP. A guided tour into subcellular colocalization analysis in light microscopy. *J Microsc* 2006;224:213–232.
23. Woodcroft BJ, Hammond L, Stow JL, Hamilton NA. Automated organelle-based colocalization in whole cell imaging. *Cytometry A* 2009;75:941–950.
24. Rizk A, Paul G, Incardona P, Bugarski M, Mansouri M, Niemann A, Ziegler U, Berger P, Sbalzarini IF. Segmentation and quantification of subcellular structures in fluorescence microscopy images using Squash. *Nat Protoc* 2014;9:586–596.
25. Kreft M, Milisav I, Potokar M, Zorec R. Automated high through-put colocalization analysis of multichannel confocal images. *Comput Methods Programs Biomed* 2004;74:63–67.
26. Comeau JWD, Costantino S, Wiseman PW. A guide to accurate fluorescence microscopy colocalization measurements. *Biophys J* 2006;91:4611–4622.
27. Meijering E, Smal G, Danuser G. Tracking in molecular bioimaging. *IEEE Signal Process Mag* 2006;23:46–53.
28. Kalaidzidis Y. Multiple objects tracking in fluorescence microscopy. *J Math Biol* 2009;58:57–80.
29. Crocker JC, Grier DG. Methods of digital video microscopy for colloidal studies. *J Colloid Interface Sci* 1996;179:298–311.
30. Lund FW, Wüstner D. A comparison of single particle tracking and temporal image correlation spectroscopy for quantitative analysis of endosome motility. *J Microsc* 2013;252:169–188.
31. Chen H, Yang J, Low PS, Cheng JX. Cholesterol level regulates endosome motility via Rab proteins. *Biophys J* 2007;94:1508–1520.
32. Lakadamyali M, Rust MJ, Babcock HP, Zhuang X. Visualizing infection of individual influenza viruses. *Proc Natl Acad Sci USA* 2003;100:9280–9285.
33. Jeon JH, Tejedor V, Burov S, Barkai E, Selhuber-Unkel C, Berg-Sørensen K, Oddershede L, Metzler R. In vivo anomalous diffusion and weak ergodicity breaking of lipid granules. *Phys Rev Lett* 2011;106:048103.
34. Tolić-Nørrelykke IM, Munteanu EL, Thon G, Oddershede L, Berg-Sørensen K. Anomalous diffusion in living yeast cells. *Phys Rev Lett* 2004;93:078102.
35. Brangwynne CP, Koenderink GH, MacKintosh FC, Weitz DA. Intracellular transport by active diffusion. *Trends Cell Biol* 2009;19:423–427.
36. Weiss M, Elsner M, Kartberg F, Nilsson T. Anomalous subdiffusion is a measure for cytoplasmic crowding in living cells. *Biophys J* 2004;87:3518–3524.
37. Guigas G, Weiss M. Sampling the cell with anomalous diffusion – the discovery of slowness. *Biophys J* 2008;94:90–94.
38. Lund FW, Lomholt MA, Solanko LM, Bittman R, Wüstner D. Two-photon time-lapse microscopy of BODIPY-cholesterol reveals anomalous sterol diffusion in Chinese Hamster ovary cells. *BMC Biophys* 2012;5:20.
39. Qian H, Sheetz MP, Elson EL. Single particle tracking. Analysis of diffusion and flow in two-dimensional systems. *Biophys J* 1991;60:910–921.
40. Brandt S. *Datenanalyse*. Heidelberg and Berlin: Spektrum Verlag; 1999.
41. Kleman M, Lavrentovich OD. *Soft Matter Physics. An Introduction*. New York: Springer; 2003.
42. Goldstein H. *Classical Mechanics*. New York: Addison-Wesley; 1980.
43. Gonzalez RC, Woods RE. *Digital Image Processing*. Upper Saddle River, NJ: Prentice Hall Inc.; 2002 Chapter 11, pp. 675–683.
44. Saxton M. Lateral diffusion in an archipelago. Single-particle diffusion. *Biophys J* 1993;64:1766–1780.
45. Helmuth JA, Burckhardt CJ, Koumoutsakos P, Greber UF, Sbalzarini IF. A novel supervised trajectory segmentation algorithm identifies distinct types of human adenovirus motion in host cells. *J Struct Biol* 2007;159:347–358.
46. Huet S, Karatekin E, Tran VS, Fanget I, Cribier S, Henry JP. Analysis of transient behavior in complex trajectories: application to secretory vesicle dynamics. *Biophys J* 2006;91:3542–3559.
47. Armitage P, Berry G, Matthews JNS. *Statistical Methods in Medical Research*, 4th edn. Oxford, UK; Berlin, Germany: Blackwell Sciences; 2002.
48. Ferrari R, Manfroi AJ, Young WR. Strongly and weakly self-similar diffusion. *Phys D* 2001;154:111–137.

49. Spandl J, White DJ, Peychl J, Thiele C. Live cell multicolor imaging of lipid droplets with a new dye, LD540. *Traffic* 2009;10: 1579–1584.
50. Schwarz G. Estimating the dimension of a model. *Ann Stat* 1978;6:461–464.
51. Wagenmakers E-J, Farrell S. AIC model selection using Akaike weights. *Psychon Bull Rev* 2004;11:192–196.
52. Daddysman MK, Fecko CJ. Revisiting point FRAP to quantitatively characterize anomalous diffusion in live cells. *J Phys Chem* 2013;117:1241–1251.
53. Türkcan S, Masson J-B. Bayesian decision tree for the classification of the mode of motion in single-molecule trajectories. *PLoS One* 2013;8:e82799.
54. Türkcan S, Alexandrou A, Masson J-B. A Bayesian inference scheme to extract diffusivity and potential fields from confined single-molecule trajectories. *Biophys J* 2012;102:2288–2298.
55. Nielsen GK, Dagnaes-Hansen F, Holm IE, Meaney S, Symula D, Andersen NT, Heegaard CW. Protein replacement therapy partially corrects the cholesterol-storage phenotype in a mouse model of Niemann-Pick type C2 disease. *PLoS One* 2011;6:e27287.
56. Diaz E, Ayala G, Diaz ME, Gong LW, Toomre D. Automatic detection of large dense-core vesicles in secretory cells and statistical analysis of their intracellular distribution. *IEEE/ACM Trans Comput Biol Bioinform* 2010;7:2–11.
57. Wüstner D. Mathematical analysis of hepatic high density lipoprotein transport based on quantitative imaging data. *J Biol Chem* 2005;280:6766–6779.
58. Mattfeldt T. Explorative statistical analysis of planar point processes in microscopy. *J Microsc* 2005;220:131–139.
59. Younge K, Christenson C, Bohara A, Crnkovic J, Saulnier P. A model system for examining the radial distribution function. *Am J Phys* 2004;72:1247–1250.
60. Chen FW, Li C, Ioannou YA. Cyclodextrin induces calcium-dependent lysosomal exocytosis. *PLoS One* 2010;5:e15054.
61. Lachmanovich E, Shvartsman DE, Malka Y, Botvin C, Henis YI, Weiss AM. Co-localization analysis of complex formation among membrane proteins by computerized fluorescence microscopy: application to immunofluorescence co-patching studies. *J Microsc* 2003;212:122–131.
62. Morrison IE, Karakikes I, Barber RE, Fernandez N, Cherry RJ. Detecting and quantifying colocalization of cell surface molecules by single particle fluorescence imaging. *Biophys J* 2003;85:4110–4121.
63. Semrau S, Holtzer L, Gonzalez-Gaitan M, Schmidt T. Quantification of biological interactions with particle image cross-correlation spectroscopy (PICCS). *Biophys J* 2011;100:1810–1818.
64. Cheezum MK, Walker WF, Guilford WH. Quantitative comparison of algorithms for tracking single fluorescent particles. *Biophys J* 2001;81:2378–2388.
65. Pipalia NH, Hao M, Mukherjee S, Maxfield FR. Sterol, protein and lipid trafficking in Chinese hamster ovary cells with Niemann-Pick type C1 defect. *Traffic* 2006;8:130–141.
66. Mbua NE, Flanagan-Steet H, Johnson S, Wolfert MA, Boons GJ, Steet R. Abnormal accumulation and recycling of glycoproteins visualized in Niemann-Pick type C cells using the chemical reporter strategy. *Proc Natl Acad Sci USA* 2013;110:10207–10212.
67. Bucci C, Thomsen P, Nicoziani P, McCarthy J, van Deurs B. Rab7: a key to lysosome biogenesis. *Mol Biol Cell* 2000;11:467–480.
68. Rocha N, Kuij C, van der Kant R, Janssen L, Houben D, Janssen H, Zwart W, Neefjes J. Cholesterol sensor ORP1L contacts the ER protein VAP to control Rab7-RILP-p150 Glued and late endosome positioning. *J Cell Biol* 2009;185:1209–1225.
69. Wüstner D. Quantification of polarized trafficking of transferrin and comparison with bulk membrane transport in hepatic cells. *Biochem J* 2006;400:267–280.
70. Bains M, Heidenreich KA. Live-cell imaging of autophagy induction and autophagosome-lysosome fusion in primary cultured neurons. *Methods Enzymol* 2009;453:145–158.
71. Hailey DW, Lippincott-Schwartz J. Using photoactivatable proteins to monitor autophagosome lifetime. *Methods Enzymol* 2009;452:25–45.
72. Targett-Adams P, Chambers D, Gledhill S, Hope RG, Coy JF, Girod A, McLauchlan J. Live cell analysis and targeting of the lipid droplet-binding adipocyte differentiation-related protein. *J Biol Chem* 2003;278:15998–16007.
73. Lajoie P, Snapp EL. Formation and toxicity of soluble polyglutamine oligomers in living cells. *PLoS One* 2010;5:e15245.
74. Wüstner D, Solanko LM, Lund FW, Sage D, Schroll JA, Lomholt MA. Quantitative fluorescence loss in photobleaching for analysis of protein transport and aggregation. *BMC Bioinform* 2012;13:296.
75. Boucrot E, Saffarian S, Massol R, Kirchhausen T, Ehrlich M. Role of lipids and actin in the formation of clathrin-coated pits. *Exp Cell Res* 2006;312:4036–4048.
76. Jagaman K, Kuwata H, Touret N, Collins R, Trimble SW, Danuser G, Grinstein S. Cytoskeletal control of CD36 diffusion promotes its receptor and signaling function. *Cell* 2011;146:593–606.
77. Hess ST, Gould TJ, Gudheti MV, Maas SA, Mills KD, Zimmerberg J. Dynamic clustered distribution of hemagglutinin resolved at 40 nm in living cell membranes discriminates between raft theories. *Proc Natl Acad Sci USA* 2007;104:17370–17375.
78. Larsen LB, Ravn P, Boisen A, Berglund L, Petersen TE. Primary structure of EPV20, a secretory glycoprotein containing a previously uncharacterized type of domain. *Eur J Biochem* 1997;243:437–441.
79. Maxfield FR, Wüstner D. Analysis of cholesterol trafficking with fluorescent probes. *Methods Cell Biol* 2012;108:367–393.
80. Edelsbrunner H, Kirkpatrick D, Seidel R. On the shape of a set of points in the plane. *IEEE Trans Inform Theory* 1983;29:551–559.
81. Beatriz PL, Alberto RC. Generalizing the convex hull of a sample: The R package alphahull. *J Stat Softw* 2010;34:1–28.
82. Thévenaz P, Ruttimann UE, Unser M. A pyramid approach to subpixel registration based on intensity. *IEEE Trans Image Process* 1998;7:27–41.

SpatTrack, an imaging toolbox for analysis of vesicle motility and distribution in living cells

Frederik W. Lund^{1,4}, Maria Louise V. Jensen¹, Tanja Christensen¹, Gitte K. Nielsen², Christian W. Heegaard³ and Daniel Wüstner^{*,1}

¹Department of Biochemistry and Molecular Biology University of Southern Denmark, DK-5230 Odense M, Denmark. ²Department of Biomedicine and ³Department of Molecular Biology and Genetics, University of Aarhus, DK-8000 Aarhus C., Denmark. ⁴Weill Medical College of Cornell University, York Ave. 1300, 10066 New York, USA

Running title: Imaging toolbox for vesicle motility and distribution

*Address correspondence to: Daniel Wüstner, Department of Biochemistry and Molecular Biology, University of Southern Denmark, Campusvej 55, DK-5230 Odense M, Denmark
Tel. +45-6550-2405, Fax +45-6593-2781, e-mail: wuestner@bmb.sdu.dk

Supplementary Information

Supplementary Methods

SpatTrack includes four analytical models for the MSD of the particle trajectories of increasing complexity 1) Brownian diffusion (model 1; Eq. 2); 2) Brownian diffusion plus flow (model 2; Eq. 3); 3) anomalous diffusion (model 3; Eq. 4) and 4) anomalous diffusion plus flow (model 4; Eq. 5). To assist the user in selecting the appropriate model for a given experiment we developed a decision tree, Fig. 2 in the main text. The decision tree is based on three criteria 1) the magnitude of the standard error (SE) of each of the fitted parameters, 2) the Bayesian information criterion (BIC) and 3) analysis by the radius of gyration (RoG) to determine if there are one or more particle populations. The first two steps in the decision tree proceeds as follows. First each of the four diffusion models are fitted to the MSD and the mean fitted value and the SE of each parameter is calculated. If the SE is more than 10 times larger than the mean parameter value for one or more parameters this model is excluded from further analysis. For example if the MSD is fit to model 2 describing diffusion plus flow and the fitted velocity is $1 \pm 10 \mu\text{m/s}$ this model is discarded from further analysis. Second, the remaining models are evaluated by the BIC. As described in the main text, the BIC analysis favors models with a smaller sum of squared residuals between the fitted curve and the data but penalizes models with more free parameters. Thus, ideally, the BIC should find the model with fewest possible free parameters which describes the data.

To determine how efficiently the two first steps of the decision tree can distinguish diffusion plus flow (models 2 or 4) from Brownian or anomalous subdiffusion (models 1 or 3) we performed a detailed analysis of simulated trajectories of diffusion plus flow (model 2) with variable diffusion constants ranging from $0.001 - 1 \mu\text{m}^2/\text{s}$ and velocities ranging from $0.1 - 1 \mu\text{m/s}$. For each parameter composition the ensemble averaged MSD was calculated from 100 trajectories of 100 steps and the percentage of MSDs correctly classified as diffusion plus flow was determined from 100 simulations for each parameter composition. As shown in Fig. S1A, close to 100% of the MSDs were correctly classified when the velocity was sufficiently large compared to the diffusion constant. On the other hand, when the diffusion constant was large relative to the velocity, the percentage of correctly classified MSDs decreased significantly (see lower

left corner of Fig. S1A). Decreasing the rate of position updates (frames/second) from 10 position updates per second to 1 improved the percentage of correctly classified MSDs from ~45% to ~75% (compare Fig. S1A with Fig. S1B). Thus, for most parameter combinations, calculation of the SE of each fitted parameter followed by analysis by the BIC correctly classified the MSD as diffusion plus flow for more than ~80% of the simulated trajectories. Importantly, this step does not distinguish between Brownian diffusion plus flow (model 2) and anomalous diffusion plus flow (model 4). To distinguish between these two models the user must proceed to follow the decision tree (Fig. 2 in the main text). Additionally, we tested how efficiently the decision tree could distinguish MSDs for trajectories moving by Brownian diffusion from the three other models. Here particles were simulated with different diffusion constants ranging from 0.001 to 1 $\mu\text{m}^2/\text{s}$. In total 100 MSDs were analyzed, where each MSD was the ensemble averaged MSD of 100 trajectories of 100 steps. As the statistical uncertainty of the MSD increases with increasing lag-time, we chose to analyze the MSDs for different lag-times ranging from 10 frames to 100 frames. This showed that analysis by the SE followed by BIC analysis classified more than 75% of these MSDs as Brownian diffusion (model 1) or anomalous diffusion (model 3). This is illustrated in Fig. S1C showing the percentage of MSDs classified as Brownian or anomalous diffusion for different diffusion constants and MSD lengths. Of the trajectories classified as Brownian diffusion or anomalous diffusion, approximately 1/3 was classified as Brownian diffusion while 2/3 of them were classified as anomalous diffusion. Interestingly, the BIC analysis was not affected by the length of the MSD. However, MSDs from trajectories of Brownian motion rarely had an anomalous exponent, α , smaller than 0.9. Thus, we empirically chose to classify anomalous MSDs with $\alpha > 0.9$ as Brownian diffusion. Particularly, we found that for MSDs with a length corresponding to less than 50% of the total trajectory length $\alpha > 0.9$ for close to 100% of the MSDs. Thus, in conclusion, the process described in the decision tree for Brownian/anomalous diffusion can recognize Brownian diffusion with more than 75% accuracy.

Fraction of free cholesterol and of Alexa488-NPC2 found in the lysosomes

In order for the NPC2 deficient fibroblasts to accumulate cholesterol they were grown in normal growth medium with 10% FBS until 90% confluence. Then the cells were plated on microscope dishes and grown for another 48 hours in the same medium. For the following discussion we shall refer to this as time $t = 0$. Subsequently, to evaluate whether incubation with functional NPC2 could rescue cholesterol efflux the cells were grown in growth medium where FCS was exchanged with lipoprotein deficient serum (LPDS) and with 100 nM NPC2. To quantify the amount of free cholesterol, the cells were labeled with filipin as described in Materials and Methods. Fig. S2A shows an example of a filipin-labeled cell at the beginning of the experiment, while Fig. S2B shows an example after additional 48 hours of growth in LPDS without functional NPC2. In Fig. S2C a cell after 48 hours of growth in LPDS supplemented medium with 100 nM functional NPC2 is shown. Clearly, NPC2 reduces the filipin intensity in the lysosomal storage organelles (LSOs) significantly. We calculated the fraction of integrated filipin intensity in the LSOs with respect to the total integrated filipin intensity of the cells. This is shown in Fig. S2D, after 0 and 48 hours incubation in LPDS in the presence and absence of NPC2.

In NPC disease fibroblasts the degradative pathway is aberrated and forms the LSOs, where cholesterol and other lipids accumulate [1]. Alexa488-NPC2 given to cells in LPDS at a concentration of 100 nM becomes enriched in vesicles pre-labeled with rhodamine-dextran (Rh-dextran), a bulk endocytosis marker, which accumulates in LE/LYSs after incubation overnight in many cell types [2]. Transport of Alexa488-NPC2

to the LE/LYSs follows a slow single exponential process with a half-time of 24 hours (Fig. S2F). When cells were preincubated with Alexa488-NPC2 for 48 hrs followed by incubation in medium without NPC2, some Alexa488-NPC2 vanished, initiating NPC2 release from the cells (i.e., about 35% with a half-time of 19 hrs, Fig. S2G). Thus, the majority of internalized NPC2 protein remains in the endo-/lysosomal system for a prolonged time.

Spatial pattern analysis using SpatTrack

SpatTrack includes two measures to determine whether the tracked particles are accumulating, repulsive or randomly distributed, the nearest neighbor (NN) and the radial distribution function (RDF) analyses. In the GUI for NN analysis Fig. S3A, the average distance between the tracked particles and their respective NN are compared to the average NN distance of a random point distribution. The ratio of both measures gives the ANN (see Eqs. 11 and 12), which is ANN = 1 for a random particle distribution. If ANN < 1 or ANN > 1, the tracked particles are accumulating or repulsing each other, respectively. For the example shown in Fig. S3A, the ANN = 1.08 ± 0.02 which indicates that the particles are randomly distributed on the NN length scale. The histograms shown in Fig. S3A were calculated from the determined position of vesicles containing Alexa488-NPC2 in a human skin fibroblast or from a random distribution of the same number of particles in the same cell geometry. The average NN distance in this example was 2.08 and 1.92 μm for the tracked and random particles, respectively. This result yields an ANN of 2.08/1.92 = 1.08 which indicates that on the NN length scale, the tracked particles are close to randomly distributed. Notice that the pixel size is 0.222 μm and the estimated mean particle size is 4 pixels. Thus, the minimum particle-particle distance due to the tracking method is 0.888 μm . From this difference we conclude that the particle detection or enhancement method does not influence the NN analysis. While the NN analysis yields information about the potential interaction between the particles it is limited to the length scale of the distance between a particles and the particle closest to it. However, in many situations spatial patterns may emerge over longer distances. Analysis using the RDF was implemented to detect such patterns. The images in Fig. S3B show the distribution of the tracked particles and a random distribution of particles, shown as blue dots, in the cell geometry. From this one can determine the number of particles within a range of distances from a reference particle. Averaged over all particles this gives the RDF denoted by $\langle F(r) \rangle$ in Eq. 13. Subsequently, any inter-particle interaction may be determined by the ratio $g(r) = \langle F_{\text{obs}}(r) \rangle / \langle F_{\text{rand}}(r) \rangle$, where $\langle F_{\text{obs}}(r) \rangle$ and $\langle F_{\text{rand}}(r) \rangle$ are the radial distribution functions for the observed particles and the randomly distributed particles, respectively. Hence, $g(r) = 1$ for a random distribution of particles, while $g(r) < 1$ and $g(r) > 1$ indicate repulsion and clustering, respectively. The plot in the lower left corner of Fig. S3B show the RDF for the example distribution for the observed and randomly distributed particles in black and blue, respectively. The RDFs were calculated within a radius of 10 μm and the plot in the lower right corner shows $g(r)$ as a function of radius. From this it can be seen that for this particular cell the particles appear to be randomly distributed at distances shorter than ~2 μm , which agrees with the result of the NN analysis. However, for distances longer than 2 μm , $g(r)$ increases to ~1.6 indicating some degree of clustering on longer distances.

Calculation of the area occupied by NPC2 containing endosomes

A major purpose of the SpatTrack suite is to easily couple particle tracking and spatial pattern analysis of the tracked particles in the cell geometry. For example the program allows one to determine the fractional area of the cell occupied by the tracked particles. To perform this calculation we set up a method based on the alpha shaping algorithm to

determine the area of the particles (3, 4). Initially the particles are connected by a Delaunay triangulation for which the outer boundary gives the convex hull. As shown in Fig. S4A the convex hull neatly fits around the particle cloud for a convex distribution. However, for a concave particle distribution the convex hull overestimates the area, as shown by the delaunay triangulation in Fig. S4B. Therefore we implemented an alpha shaping method to refine the area estimation. This method is based on a circle with a radius, $r = \alpha \cdot \langle NN_{obs} \rangle$, where α is a user defined constant and $\langle NN_{obs} \rangle$ is the average nearest neighbor distance calculated for the particle cloud. For each line segment in the triangulation the circle is placed at the center and line segments where the circle does not contain or touch any of the detected points are deleted. Fig. S4B shows a circle placed so it does not contain any particle coordinates while Fig. S4C shows the calculated area of the concave shape after alpha shaping. For live cell images we implemented one more restriction. Here we know that the area occupied by the detected particles cannot extend the cell shape, as shown in Fig. S4D. Therefore, any such line segments are deleted prior to alpha shaping, as shown in Fig. S4E. Finally, after performing the alpha shape optimization the area is shown in Fig. S4F.

Pixel-based co-localization analysis

The Pearson correlation coefficient (PCC) is a common measure of intensity correlations in two-channel images and is given by:

$$PCC = \frac{\sum_{i=1}^n (R_i - \bar{R})(G_i - \bar{G})}{\sqrt{\sum_{i=1}^n (R_i - \bar{R}) \times \sum_{i=1}^n (G_i - \bar{G})}}, \quad (S1)$$

where R and G represent the red and the green channel and n is the number of pixels in the image. PCC ranges from +1 for perfect co-localization over 0 for no correlation to -1 for anti-correlation (i.e., a situation where pixels of high intensity in red are always associated with low intensity in green and vice versa). Using the same notation, the Mander's overlap coefficients (MOCs) for the red and the green channel are given by:

$$M_{red} = \frac{\sum_{i=1}^n R_{i,coloc}}{\sum_{i=1}^n R_i} \quad \text{and} \quad M_{green} = \frac{\sum_{i=1}^n G_{i,coloc}}{\sum_{i=1}^n G_i}, \quad (S2)$$

Here, M_{red} and M_{green} are the overlap coefficients for the red and green channel, respectively. Thus, M_{red} is given by the summed fluorescence intensity in the red channel in pixels which contain both a red and a green response normalized to the total fluorescence intensity in the red channel and vice versa for M_{green} . In other words M_{red} is the fraction of red fluorescent pixels overlapping with green fluorescent pixels. The MOC ranges from 0 for no colocalization to +1 for full colocalization. The analysis results are presented in Fig. S5. In addition, we demonstrate that fluorescent bovine NPC2, like Alexa488- or Alexa546-NPC2, was able to restore cholesterol egress from NPC2 deficient human skin fibroblasts (Fig. S5A).

References

1. Mukherjee S, Maxfield FR (2004) Lipid and cholesterol trafficking in NPC. *Biochim Biophys Acta* 1685: 28-37.
2. Mukherjee S, Ghosh, R.N., and Maxfield, F.R. (1997) Endocytosis. *Physiol Rev* 77: 759-803.
3. Edelsbrunner H, Kirkpatrick D, Seidel R (1983) On the shape of a set of points in the plane. *IEEE Transactions on Information Theory* 29: 551-559.
4. Beatriz PL, Alberto RC (2010) Generalizing the Convex Hull of a Sample: The R Package alphahull. *Journal of Statistical Software* 34.

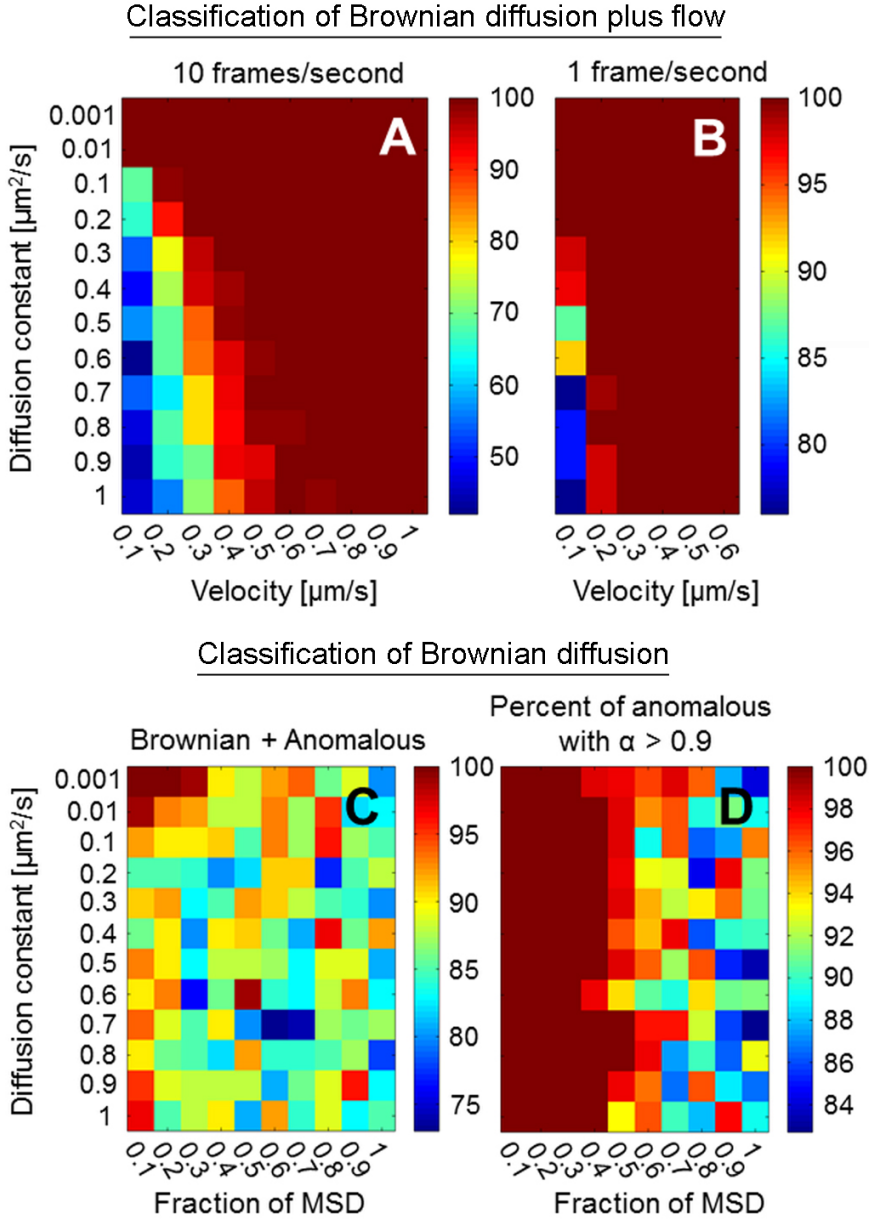


Figure S1: To test the first steps in the decision tree, additional vesicle simulations were performed, in particular of diffusion plus flow and normal/hindered diffusion. MSDs of simulated trajectories of diffusion plus flow with variable diffusion constant and/or velocity were analyzed by the standard error (SE) of the fitted parameters followed by analysis using the Bayesian information criterion (BIC). Panels A and B show the percentage of trajectories correctly classified as diffusion plus flow. Each square represents the analysis of 100 MSDs generated as the ensemble average of 100 trajectories with a length of 100 steps. For trajectories, in which the velocity was small compared to the diffusion constant, decreasing the frame rate from 10 frames/second to 1 frame/second increased the number of correctly classified trajectories. For most parameter combinations, the combined analysis of the parameter's SEs followed by BIC analysis led to a correct classification (i.e., in more than 80% of the analyzed MSDs). Additionally, the MSDs of simulated trajectories of Brownian diffusion with different diffusion constants were analyzed. Here, the procedure described in the decision tree classified 75% of the MSDs as Brownian diffusion or anomalous diffusion, see panel C. For MSDs of short lag-times close to 100% of the trajectories classified as anomalous diffusion had an anomalous exponent larger than 0.9, panel D and were, thus, classified as Brownian diffusion.

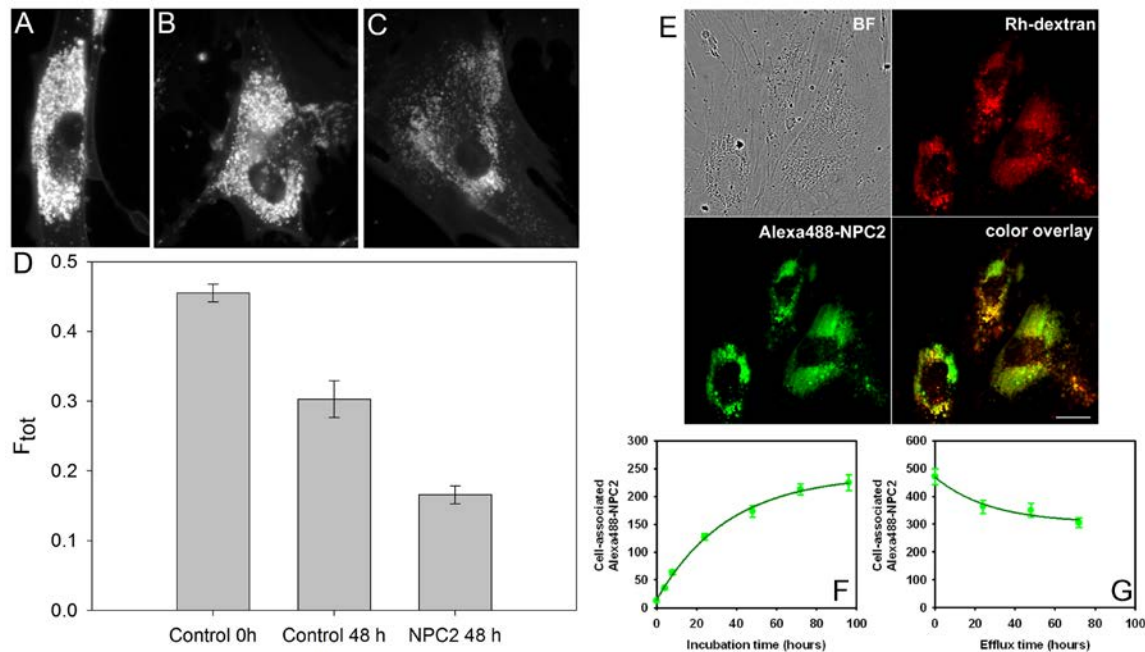


Figure S2: Filipin intensity and distribution in cells after 0 and 48 hours of growth in LPDS without NPC2, A and B, respectively and after 48 hours of growth in LDPS with 100 nM NPC2 panel C. Panel D shows the fraction of filipin in the LSO with respect to the total cellular filipin at the three different conditions. Filipin is a marker for free cholesterol. Thus, panel D shows that after 48 hours of growth without NPC2 ~34% cholesterol is effluxed while 65% cholesterol is effluxed over 48 hours in the presence of functional NPC2. Data represent mean +/- SEM of two separate experiments with each having recorded at least five fields having one to three cells per field and condition. Fluorescent NPC2 is targeted to LSOs and recycles slowly to the cell surface. E, F, Uptake of NPC2. NPC2 disease fibroblasts were incubated over night with 0.5 mg/ml Rh-Dextran to prelabel LSOs. Cells were subsequently incubated with 100 nM Alexa488-NPC2 in LPDS containing medium for the incubated time points (72 hours in E). Fluorescence of Alexa488-NPC2 in the LSOs was quantified as described in Materials and Methods and plotted as function of time (F, symbols, mean \pm SE; n=30). The data was fitted to a mono-exponential function without residual (F, green line). After 48hours of uptake as described above, cells were switched to medium containing LPDS but no NPC2 protein and kept there for the indicated time points. Fluorescence of Alexa488-NPC2 in the LSOs was quantified as described above (G, symbols, mean \pm SE; n=16) and fitted to a mono-exponential decay function with residual. On average 3-6 cells were imaged per field giving the indicated number of images, i.e., n, per time point. Bar, 10 μ m.

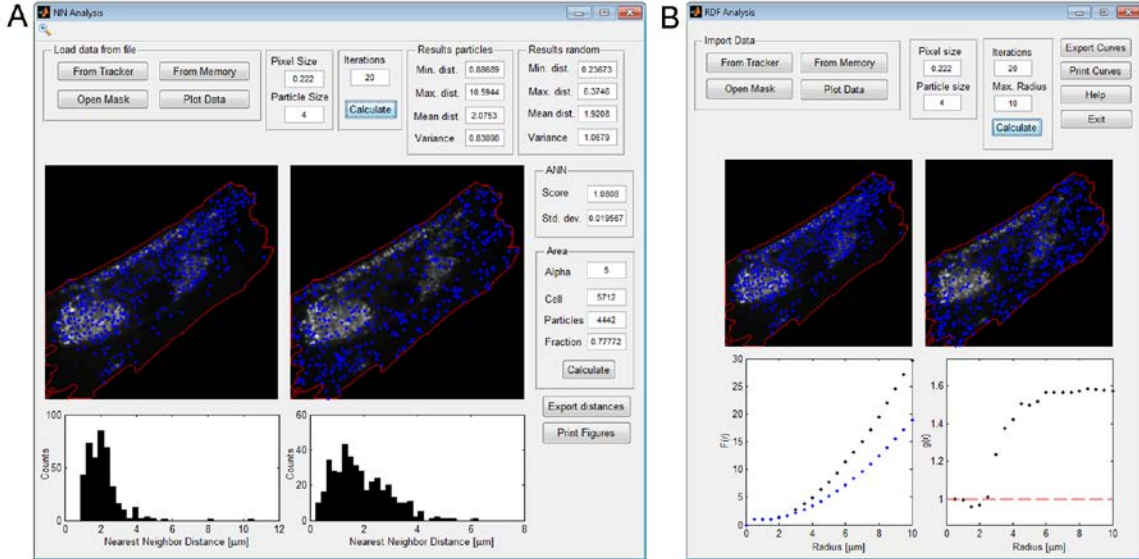


Figure S3: GUI for determining nearest neighbors (NN; A) and the radial distribution function (RDF; B). The histograms of NN distances are placed under the cell images for the tracked (A, lower left bar plot) and simulated particle distribution (A, lower right bar plot), respectively. In the RDF analysis (B) the number of particles within a distance from a reference particle is compared to the same measure for the random particles. This yields a function $\langle F(r) \rangle$, as defined in Eq. 9, for the tracked and random particle distribution (black and blue symbols in the lower left plot of panel B). The ratio of measured and simulated $\langle F(r) \rangle$ gives a function $g(r)$ according to Eqs. 10 and 11 with $g(r) = 1$ for a random distribution and $g(r) < 1$ or $g(r) > 1$ for a repulsive or aggregating particle population, respectively. For the particle population examined here it can be seen that $g(r) \sim 1$ for distance of less than $\sim 2 \mu\text{m}$ and $g(r) \sim 1.6$ for distances of more than $4 \mu\text{m}$, indicating vesicle aggregation over longer distances. The spatial distribution of the tracked and simulated particles is shown in the cell geometry in the central left and right image of panel A and B, respectively.

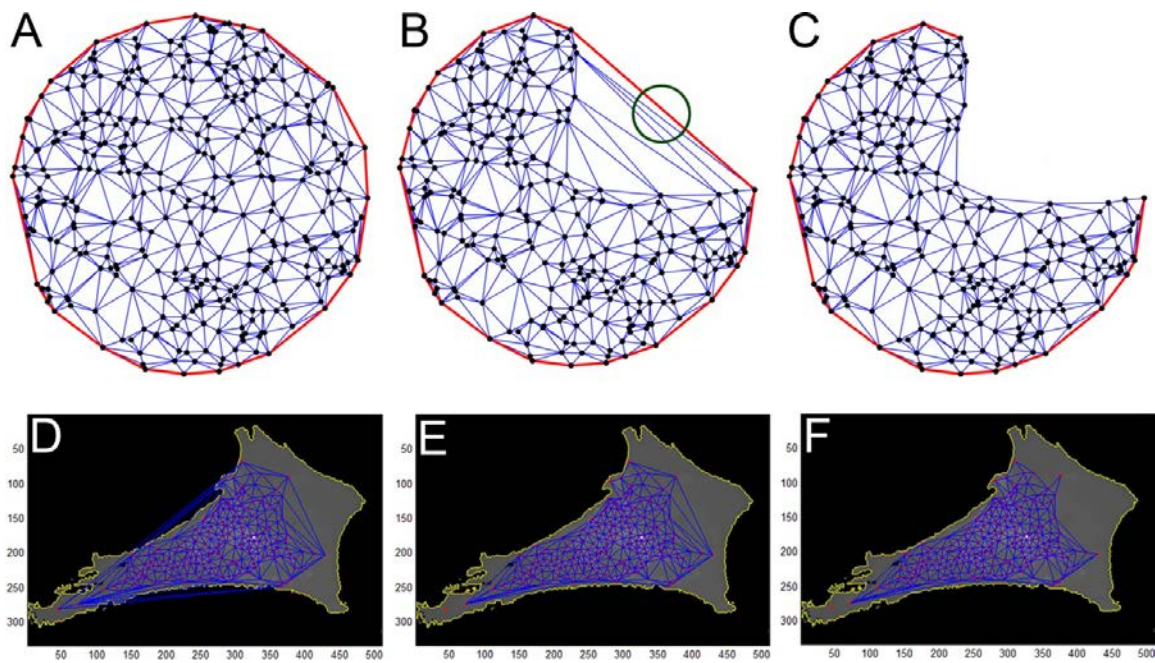


Figure S4: Illustration of the triangulation process. Panels A-C show a theoretical example while panels D-F show the result on a set of detected endosomes inside a cell. First the Delaunay triangulation is calculated for the particles. The outer rim of the triangulation is the convex hull which fits tightly around a convex particle distribution, panel A. However, for a concave particle distribution the convex hull overestimates the particle area, panel B. Next the triangulation is refined by alpha shaping. A circle with radius α is placed on each line segment (green circle in panel B) and line segments where the circle does not contain any particles are deleted. Panel C shows the area after alpha shaping. In panel D the Delaunay triangulation is shown for a distribution of endosomes inside a NPC2^{-/-} cell. Initially, line segments crossing the cell boundary are deleted as the area occupied by the endosomes cannot extend the cell geometry, compare panel D and E. Next, the alpha shape procedure is applied to generate the final triangulation, panel F. The procedure allows for calculating the fractional area occupied by the particles.

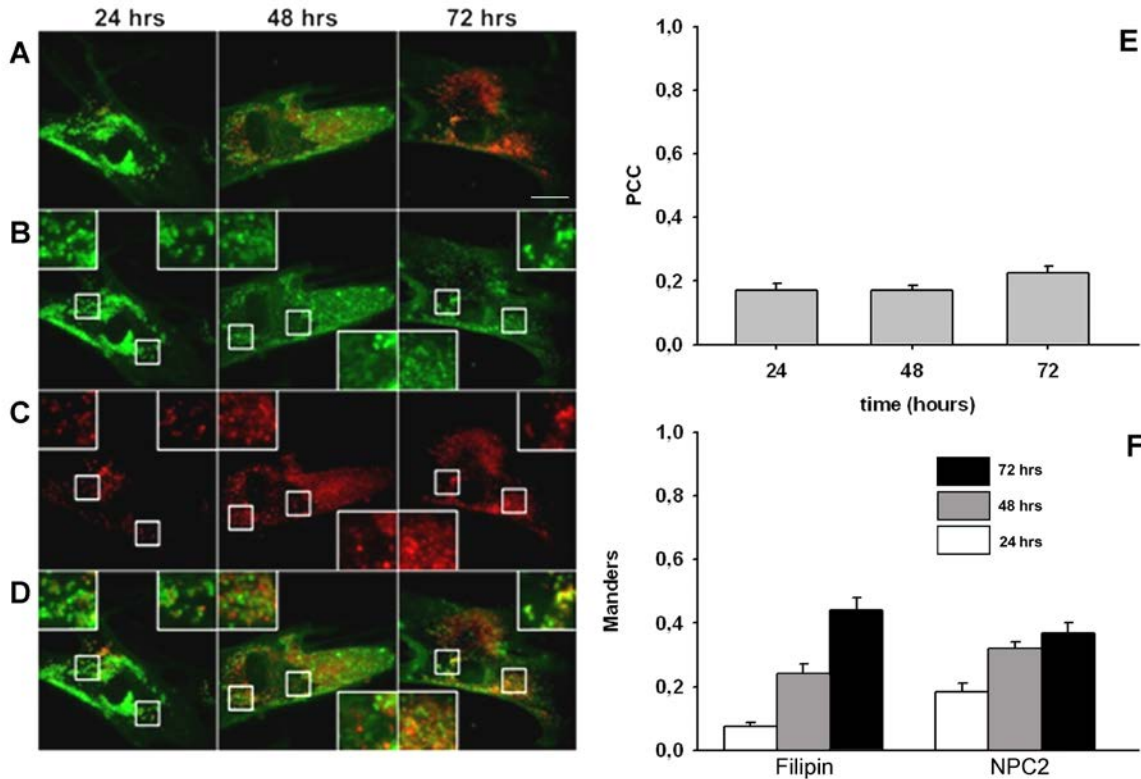


Figure S5: Pixel-based co-localization analyses of Alexa546-NPC2 and filipin. NPC2 disease fibroblasts were cultured in medium containing LDL and other lipoprotein sources before switching to medium containing LPDS and 100 nM Alexa546-NPC2 for either 24, 48 or 72 hrs. Cells were washed, fixed with PFA and stained for free cholesterol using the polyene filipin as described in Materials and Methods. Images were pseudo-colored using an appropriate LUT in ImageJ with filipin in green and Alexa546-NPC2 in red. A, a linear LUT shows the relative intensities for filipin and Alexa546-NPC2 (i.e., decreasing and increasing over time, respectively). Bar, 20 μ m. B-D, shows the same fields with enhanced contrast to highlight the low extend of co-localization between NPC2 and sterol (see also insets in B-D). E, Pearson co-localization coefficient ('PCC') and F, Mander's overlap coefficient ('Manders') calculated between the NPC2 and filipin channel after image denoising from 13 images at each time point, and the bar plots are displayed with error bars of ± 1 standard error.